On the Significance of Hydrate Formation/Dissociation during CO_2 Injection in Depleted Gas Reservoirs

Indina, V.; Fernandes, B. R.B.; Delshad, M.; Farajzadeh, R.; Sepehrnoori, K.

DOI
10.2118/218550-PA

Publication date
2024

Document Version
Final published version

Published in
SPE Journal

On the Significance of Hydrate Formation/Dissociation during CO_2 Injection in Depleted Gas Reservoirs

V. Indina[1], B. R. B. Fernandes[2], M. Delshad[1,2*], R. Farajzadeh[3], and K. Sepehrnoori[1]

[1]Hildebrand Department of Petroleum Engineering, University of Texas at Austin
[2]Center for Subsurface Energy and the Environment, University of Texas at Austin
[3]Department of Geosciences and Engineering, Delft University of Technology

Summary

The study aims to quantitatively assess the risk of hydrate formation within the porous formation and its consequences on injectivity during storage of CO_2 in depleted gas reservoirs considering low temperatures caused by the Joule-Thomson (JT) effect and hydrate kinetics. Hydrates formed during CO_2 storage operation can occupy porous spaces in the reservoir rock, reducing the rock's permeability and thus becoming a hindrance to the storage project. The aim was to understand which mechanisms can mitigate or prevent the formation of hydrates. The key mechanisms we studied included water dry-out, heat exchange with surrounding rock formation, and capillary pressure. A semicompositional thermal reservoir simulator is used to model the fluid and heat flow of CO_2 through a reservoir initially composed of brine and methane. The simulator can model the formation and dissociation of both methane and CO_2 hydrates using kinetic reactions. This approach has the advantage of computing the amount of hydrate deposited and estimating its effects on the porosity and permeability alteration. Sensitivity analyses are also carried out to investigate the impact of different parameters and mechanisms on the deposition of hydrates and the injectivity of CO_2. Simulation results for a simplified model were verified with results from the literature. The key results of this work are as follows: (1) The JT effect strongly depends on the reservoir permeability and initial pressure and could lead to the formation of hydrates within the porous media even when the injected CO_2 temperature was higher than the hydrate equilibrium temperature; (2) the heat gain from underburden and overburden rock formations could prevent hydrates formed at late time; (3) permeability reduction increased the formation of hydrates due to an increased JT cooling; and (4) water dry-out near the wellbore did not prevent hydrate formation. Finally, the role of capillary pressure was quite complex, as it reduced the formation of hydrates in certain cases and increased in other cases. Simulating this process with heat flow and hydrate reactions was also shown to present severe numerical issues. It was critical to select convergence criteria and linear system tolerances to avoid large material balance and numerical errors.

Introduction

Evidence suggests that the increase in greenhouse gas concentrations in the atmosphere is the main cause of global warming and climate change (Verheggen et al. 2014; Cook et al. 2016; Rose et al. 2017). Underground storage of CO_2 is a promising method to mitigate global energy-related emissions (Bouzalakos and Mercedes 2010). CO_2 storage and utilization projects will be critical pathways to reducing emissions and delivering climate change goals and net zero. Depleted natural gas reservoirs are identified as potential candidates for CO_2 storage because they provide a large storage capacity and already have part of the required infrastructure installed (Al Hagrey et al. 2014; Sun et al. 2016; Gauteplass et al. 2018; Hoteit et al. 2019). However, injecting CO_2 at high pressure and low temperature, into a low-pressure depleted reservoir increases the risk of CO_2 hydrate and ice formation because of the JT cooling phenomena (Oldenburg 2007; Han et al. 2010; Zatsepina and Pooladi-Darvish 2012). Such thermophysical effects can significantly influence injectivity, which leads many researchers to conduct theoretical and experimental investigations to better understand this phenomenon and its possible risks (Zatsepina and Pooladi-Darvish 2012; Wapperom et al. 2022).

Past storage projects documented challenges with corrosion caused by impurities in the captured CO_2 and failure to achieve the target injectivity (Lewis 2022). The carbon capture and storage (CCS) project Quest in Canada required a sustained injection rate of 1.08 Mt/a for a minimum of 10 years (2010) for the approval process (Stantec Consulting 2010).

To lower the risk of injectivity loss during CCS operations, experimental and numerical studies are highly recommended for each target storage site to anticipate and reduce risks that may occur during storage operations.

Oldenburg (2007) investigated the magnitude of the JT cooling during CO_2 injection in Sacramento Valley, California, USA. In their study, they investigated constant injection pressure scenarios and constant injection rates with low and high permeabilities. They used the TOUGH2/EOS7C simulator and validated their results with experimental data. They concluded that the JT cooling would not pose an issue for their field considering its permeability range, rate, and the heating of CO_2 through the pipes and wellbore. However, the authors do advise that care must be taken when injecting cryogenic CO_2. The results from Oldenburg (2007) were supported by the analytical solution developed by Mathias et al. (2010). However, the analytical solution considered three major assumptions—constant thermophysical properties, single-phase flow, and steady-state pressure field.

Creusen (2018) did a comprehensive work focusing on the "near wellbore effect" during CO_2 sequestration in depleted gas reservoirs. They used numerical simulation to model the JT effect, the salt precipitation, and the hydrate formation using TOUGH2-ECO2MG and CMG-GEM. In the research, it was concluded that the CO_2 injection rate, injection temperature, reservoir permeability, and initial reservoir pressure are all critical parameters for JT cooling and hydrate formation. They observed cooling as high as 15–20°C in some cases due to the JT effect.

*Corresponding author; email: delshad@mail.utexas.edu

This paper (SPE 218550) was accepted for presentation at the SPE Conference at Oman Petroleum & Energy Show, Muscat, Oman, 22–24 April 2024, and revised for publication. Original SPE manuscript received for review 12 May 2024. Revised manuscript received for review 10 September 2024. Paper peer approved 17 September 2024.

One of the first quantitative studies on the hydrate decomposition kinetics was done by Kim et al. (1987) for methane hydrates. The model presented by the authors considered a transient hydrate decomposition based on a fugacity gradient. In their model, the authors assumed the hydrate to be composed of spherical grains with a reactive layer. As the hydrate decomposes, a layer of gas ends up surrounding the hydrate grain. The triple-point equilibrium fugacity is considered at the hydrate grain's surface. Englezos et al. (1987) presented a mechanistic model for the formation and growth of methane and ethane hydrates. The authors assumed the hydrates to be composed of spherical grains surrounded by an adsorption reactive layer that is surrounded by a stagnant liquid diffusion layer in which the gas diffuses from the fluid bulk to the hydrate reactive surface. The diffusion rate and adsorption rates are the same at steady state, and the reaction is assumed to be of first order in the gas concentration due to excess water. This all leads to a model that relates the rate of hydrate formation to the difference between the dissolved gas fugacity and the triple point equilibrium fugacity. This model is very similar to the one proposed by Kim et al. (1987) for dissolution, in the reverse direction, but the gas fugacity is replaced by the dissolved gas fugacity. Shindo et al. (1993a, 1993b) proposed a kinetic model for the CO_2 hydrate formation. This model assumed that water would dissolve into liquid CO_2 and then react. A first-order reaction was considered, but the water concentration in the liquid CO_2 was used instead of a fugacity. Ahmad et al. (2019) investigated the nucleation of CO_2 hydrate in hydrate-bearing formations for CCS with a nonisothermal approach that considered the time-dependent kinetics for hydrate growth. The authors assumed the hydrate formation to depend on CO_2 solubility. The authors observed pressure propagation delay with the reduction in permeability which resulted in less propagation of the CO_2 hydrate front. Furthermore, the authors observed the exothermic nature of the hydrate formation to slow the hydrate growth. It is important to mention that the presence of a solid surface, such as the solid matrix, plays an important role in gas hydrate nucleation, which is neglected by many of the models mentioned before. A comprehensive review of the gas hydrate nucleation in the presence of solid surfaces is presented by Nguyen et al. (2020). The authors point out the complexity of wetting in porous structures and its importance on hydrate nucleation. The review indicates that high water saturation can hinder hydrate nucleation and points out the importance of surface chemistry and pore size. The authors indicate that mesopores with moderate wettability are optimal for hydrate growth.

A sequence of series of developments in hydrate modeling and simulation was done by researchers from the Lawrence Berkeley National Laboratory. Moridis et al. (2008) presented the TOUGH + HYDRATE v1.0 simulator, developed for modeling the nonisothermal methane hydrate release from natural bearing formations. TOUGH + HYDRATE v1.0 could handle both equilibrium and kinetics hydrate reactions and used the model from Kim et al. (1987) for the kinetics case and is based on the work from Moridis et al. (1998). Developed later, TOUGH + HYDRATE v2.0 (Moridis et al. 2019) is a fully implicit nonisothermal compositional simulator and can describe all 15 possible thermodynamic states of the methane hydrate.

Uddin et al. (2008b) presented a unified gas hydrate model with the thermal reservoir simulator CMG STARS for CO_2 storage (Uddin et al. 2008a). The authors considered methane and CO_2 hydrate as well as ice formation. The authors considered the injection of CO_2 in four different formations. However, the formations considered a half-rectangular geometry leading to a linear (2D) flow. The JT effects were not addressed by the authors and no JT cooling could be observed on their temperature fields. An increase in the reservoir pressure was observed when hydrates were formed, and such an effect was less pronounced for high-permeability formations.

Zatsepina and Pooladi-Darvish (2011) proposed the injection of CO_2 in depleted gas reservoirs in northern Alberta. The authors considered the formation of CO_2 hydrates as a beneficial trapping mechanism for the permanent storage of CO_2. The authors considered CMG STARS in their study and assumed fast intrinsic hydrate kinetics. The authors make no mention of JT effects or nonideal enthalpy in their calculation, but the results suggest that these were not considered in their study because temperature did not seem to be affected by the pressure profile resulting in no cooling zone. On the other hand, an increase in temperature could be observed as hydrates were formed due to the hydrate formation's exothermic reaction. From their results, the formation of hydrate did not plug the formation with a maximum hydrate saturation of 0.32.

Janicki et al. (2011) developed an in-house simulator (UMSICHT HyRes) to model the recovery of methane hydrate while storing CO_2 as hydrate. Their model considers a concentration-based hydrate formation kinetic model. Additionally, their model was compared with CMG STARS.

Lin et al. (2020) presented history-matched, laboratory-scale experimental data (Shu and Lee 2016) of a process of methane hydrate replacement by CO_2 hydrate, using CMG STARS for their study. CMG STARS was also used to history match experiments and later optimization of the in-situ CO_2 generation processes with the use of urea, which also considered reaction kinetics and thermal effects (Hussain 2021; Hussain et al. 2021, 2023; Wu et al. 2023).

Gauteplass et al. (2020) presented an experimental study of CO_2 hydrate inhibition and remediation. The experimental results indicated injectivity loss during the formation of hydrates. The authors observed that methanol injection and thermal stimulation can dissociate hydrate plugs. Thermal stimulation was the most effective remediation method for near-zero permeability conditions.

You et al. (2019), Ruppel and Waite (2020), and Sholihah and Sean (2021) performed literature reviews to understand the mechanisms of hydrate formation and dissociation. Their studies address challenges in the modeling of gas hydrate dissociation and formation, with a primary focus on methane production. These studies highlight the importance of coupling multiphase flow and multicomponent reactive transport with geological history.

Burke (2011) and Xu et al. (2020) conducted studies on gas injectivity using an analytical approach. Burke (2011) studied the impact of rock permeability on CO_2 injectivity and containment during storage operations. Xu et al. (2020) conducted their study at a finer resolution compared with Burke (2011), investigating the effect of pore size distribution on gas injectivity.

Machado et al. (2023) published a comprehensive modeling paper to highlight injectivity assessments in CCS projects considering all the possible risks, including the hydrate formation. Understanding the CO_2 thermodynamics is important for an accurate forecast of the injectivity of the wells for (1) planning the flexibility of the storage projects, such as the number of wells and the need for pressure management wells; (2) whether there is a need for surface storage tanks for temporary storage of captured CO_2; and (3) mitigation strategy for hydrate formation by heating the CO_2 source, using chemicals, or change in the injection strategy (Yamada et al. 2024).

Aghajanloo et al. (2024) performed a comprehensive theoretical study about the impact of CO_2 hydrates on injectivity during CO_2 storage in depleted gas reservoirs. This study also discussed how pore size, rock minerals, water saturation, and impurities in the CO_2 stream affect hydrate formation in the reservoir. Moreover, this study found that capillary heterogeneity can cause capillary-driven backflow where water flows back to the direction of the injector. This phenomenon can impact the dynamic of water dry-out and hydrate formation during CO_2 injection. Al Maqbali et al. (2023) also studied the reaction kinetics such as activation energy and reaction frequency factor for several geochemical reactions while injecting CO_2 in a saline aquifer for carbon storage through mineralization in southwest Oklahoma. Temperature sensitivity was also performed to analyze the impact of temperature on CO_2 mineralization and generation of hydrates.

Singh et al. (2020) presented a nonisothermal model for the fluid flow of gas and water in hydrate-bearing formations. The model from Kim et al. (1987) was modified to account for hydrate kinetics. The model considered only 1D linear flow and the authors assumed the JT

effect to be negligible in such scenarios, thus not including it in their model. The main objective of their study was to observe the impact of four parameters (reservoir porosity, initial water saturation, initial reservoir temperature, and injection pressure) on the storage of CO_2 in the form of hydrate within the porous formation. According to their results, changes in temperature were negligible and an isothermal model could represent well their results. The study showed that the initial water saturation affects both CO_2 migration and hydrate formation. Also, a higher hydrate formation rate was observed near the injection well, with the amount of CO_2 hydrates increasing with an increase in injection pressure and a decrease in initial reservoir temperature.

Coelho et al. (2021a, 2021b) developed a compositional wellbore simulator for modeling the hydrate deposition risk assessment which could handle impurities, inhibitors, water evaporation, and the salinity effect. This was an equilibrium-based approach that used the chemical potential equality as proposed originally by van der Waals and Platteeuw (1958) and followed by other authors (Parrish and Prausnitz 1972; Munck et al. 1988). Coelho et al. (2021a, 2021b) combined the IPHREEQc geochemistry module with a cubic equation of state for modeling the phase equilibrium.

Furthermore, Kumari et al. (2022) presented a comparison of different machine learning and genetic programming techniques to estimate the thermodynamic conditions of hydrate formation based on pressure, temperature, and gas molecular weight. Also, Yamada et al. (2024) developed a physics-based machine learning model to assess the risk of hydrate formation during CO_2 storage in depleted gas reservoirs. It is the first machine learning model applied to assess the risk of hydrate formation from injection conditions (injection rate and temperature) and reservoir properties (thickness, permeability, temperature, porosity, and water saturation). The authors observed deep neural network models to present the best predictive ability and observed injection rate, injection temperature, initial reservoir pressure, and reservoir permeability to have the highest impact on the risk of hydrate formation. However, the approach proposed by the authors could not quantify the amount of the formed hydrates.

In this paper, a semicompositional thermal reservoir simulator was considered to assess the CO_2 hydrate risk and its consequences in a depleted gas reservoir considering the JT effect. This research is focused on modeling hydrate formation with a numerical simulator (CMG-STARS) using the formation/dissolution kinetic reactions to predict the hydrate formation and estimate the amount of hydrates formed and subsequent impact on injectivity. It is important to mention that storing CO_2 as hydrate is not a goal of this research. Instead, it is our goal to understand how the injectivity can be compromised due to the formation of hydrates, even when injecting CO_2 with a temperature above hydrate conditions. Sensitivity analysis of different parameters and key physical phenomena such as heat exchange with surrounding rock formation, capillary pressure, and permeability reduction are also considered. To the best of our knowledge, an in-depth study of the combined impacts of JT cooling and hydrate formation and deposits during CO_2 storage into depleted gas reservoirs has not been presented in the literature. Thus, this study aims to contribute to this topic.

Methodology

CMG-STARS (version 2023.30) is used to simulate the JT cooling effect and hydrate formation in the depleted low-pressure reservoir model. Practically, we can calculate the temperature drop because of the cooling effect with the JT coefficient. The following defines the JT coefficient:

$$\mu_{\mathrm{JT}} = \left(\frac{\partial T}{\partial P}\right)_H, \tag{1}$$

where T is the temperature, P is the pressure, and H is the enthalpy. Eq. 1 indicates the dependency of the JT coefficient on the fluid enthalpy. In STARS, the gas enthalpy is computed as

$$H_g = \sum_{i=1}^{n_c} y_i H_{gi}^{\mathrm{ideal}} + H_g^{\mathrm{depart}}, \tag{2}$$

where n_c is the number of components, y_i is the mole fraction of the ith component in the gas phase, H_g is the gas phase total enthalpy, H_{gi}^{ideal} is the ideal gas enthalpy for component i, and H_g^{depart} is the gas phase departure enthalpy, which is the deviation of the gas enthalpy from the ideal gas. The ideal gas enthalpy is computed as

$$H_{gi}^{\mathrm{ideal}} = C_{pgi} T, \tag{3}$$

where C_{pgi} is the heat capacity for component i and is evaluated using the following correlation:

$$C_{pgi}^{\mathrm{ideal}} = a_0 + a_1 T + a_2 T^2 + a_3 T^3 + a_4 T^4. \tag{4}$$

The departure enthalpy is computed from the corresponding states approach (Lee and Kesler 1975) as

$$\frac{H_g^{\mathrm{depart}}}{RT_c} = \left[\frac{H_g^{\mathrm{depart}}}{RT_c}\right]^{(0)} + \left(\frac{\omega}{\omega^{(r)}}\right)\left\{\left[\frac{H_g^{\mathrm{depart}}}{RT_c}\right]^{(r)} - \left[\frac{H_g^{\mathrm{depart}}}{RT_c}\right]^{(r)}\right\}, \tag{5}$$

where ω is the mixture acentric factor, T_c is the mixture critical pressure, R is the gas constant, the superscript (0) was used to denote the simple fluid departure enthalpy, and the superscript (r) denotes the reference fluid (n-octane). Both departure enthalpies for the simple fluid and reference fluids are provided from the diagrams provided by Lee and Kesler (1975). The mixture acentric factor is obtained from a mixing rule as

$$\omega = \sum_{i=1}^{n_c} x_i \omega_i, \tag{6}$$

where x_i is the mole fraction of component i in the phase, ω_i is the acentric factor of component i, and n_c is the number of components. The mixture critical temperature is also obtained from a mixing rule as

$$T_c = \frac{1}{8V_c}\sum_{j=1}^{n_c}\sum_{i=1}^{n_c} x_i x_j \left(V_{ci}^{1/3} + V_{cj}^{1/3}\right)^3 \sqrt{T_{ci}T_{cj}}, \tag{7}$$

where T_{ci} is the critical temperature from component i, V_{ci} is the critical volume from component i, and V_c is the mixture critical volume, also obtained from a mixing rule:

$$V_c = \frac{1}{8}\sum_{j=1}^{n_c}\sum_{i=1}^{n_c} x_i x_j \left(V_{ci}^{1/3} + V_{cj}^{1/3}\right)^3. \tag{8}$$

The hydrate kinetic model considered in STARS is based on Kim et al. (1987), originally proposed for hydrate dissociation and rewritten here as

$$-\frac{dn_h}{dt} = K_d A_h \left(f_h^* - f_h^g\right), \tag{9}$$

where n_h is the number of moles of hydrate of the gas component h; A_h is the surface area of the hydrate h, which is assumed to consist of spheres; K_d is the dissociation rate constant; f_h^g is the fugacity of component h in the gas phase; f_h^* is the fugacity of component h in the gas-hydrate equilibrium; and t is the time.

In STARS, the model presented in Eq. 9 is modified by assuming that the fugacity coefficients are equal to one, the rate constant to follow the Arrhenius equation, and Raoult's law. Moreover, the same model is considered for both hydrate formation and dissociation and is rewritten in terms of hydrate concentration. Therefore, Eq. 9 is rewritten as

$$\frac{dc_h}{dt} = \left(\frac{K_d^0 A_{hs}}{\rho_w \rho_h}\right)\left(\phi S_w \rho_w\right)\left(\phi S_h \rho_h\right)\left(y_h P_g\right)\left(1 - \frac{1}{K}\right)\exp\left(-\frac{\Delta E_h}{RT}\right), \tag{10}$$

where c_h is the molar concentration of hydrate h, A_{hs} is the specific area of the hydrate h, K_d^0 is the intrinsic decomposition rate constant, ρ_w is the water density, ρ_h is the hydrate density of component h, ϕ is the porosity, S_w is the water saturation, S_h is the hydrate saturation of component h, y_h is the mole fraction of component h in the gas phase, P_g is the gas pressure, K is the equilibrium constant for the gas molecule considered, ΔE_h is the activation energy of the gas hydrate from component h, and T is the temperature. The K-values are defined by the hydrate equilibrium as the hydrate equilibrium pressure divided by the gas pressure (P_e/P_g) and are computed as

$$K = \left(\frac{r_1}{P_g} + r_2 P_g + r_3\right)\exp\left(\frac{r_4}{T - r_5}\right), \tag{11}$$

where r_1, r_2, r_3, r_4, and r_5 are fitting parameters.

The gas phase density is calculated from the Redlich-Kwong cubic equation of state (Redlich and Kwong 1949) while the aqueous phase is assumed to be slightly compressible.

The gas phase viscosity is a function of temperature and composition only and is computed as

$$\mu_g = \frac{\sum_{i=1}^{n_c} y_i \sqrt{M_i}\mu_{gi}}{\sum_{i=1}^{n_c} y_i \sqrt{M_i}}, \tag{12}$$

where M_i is the molecular weight of component i, y_i is the mole fraction of component i in the gas phase, and μ_{gi} is the viscosity of the pure component i computed as

$$\mu_{gi} = a_i T^{b_i}, \tag{13}$$

where a_i and b_i are fitting parameters.

The STARS default brine viscosity model was used.

Liquid CO_2 was observed in the reservoir conditions in our study. The simulator can model the liquid/gas equilibrium with K-values. However, severe numerical issues were observed during the phase transition, forcing us to consider the CO_2 gas and aqueous phases. While less accurate, we consider this to be a more conservative approach as the JT coefficient for the liquid CO_2 is significantly lower than that of the gas phase. In other words, more cooling is observed with the gas phase leading to more hydrates. We also observed anomalous behavior when the calculated gridblock temperature and pressure were close to the CO_2 critical point.

The K-values for water-CO_2 are obtained from Spycher et al. (2003) and for water-CH_4 are obtained from Sartini (2021).

Finally, permeability reduction can occur when hydrates and ice are formed as these will reduce porosity. The permeability change with porosity is modeled with a Kozeny-Carman relation (Moghanloo et al. 2018) as

$$k = k_0\left(\frac{\phi}{\phi_0}\right)^{c_k}\left(\frac{1-\phi_0}{1-\phi}\right)^2, \tag{14}$$

where k is the permeability, k_0 is a reference permeability evaluated at a reference porosity ϕ_0, and c_k is an exponent that controls the permeability reduction.

The injectivity is an important metric to relate the pressure increase in the well and the injection rate and it has an important application in preventing the well from reaching the fracturing pressure (Burke 2011). The injectivity can be computed as (Machado et al. 2023; de Kok 2024)

$$I = \frac{m}{P_{bh} - \overline{P}_r}, \tag{15}$$

where I is the injectivity, m is the mass injection rate, P_{bh} is the bottomhole pressure, and $\overline{P}_r$ is the average reservoir pressure.

Radial grids were used for performing the sensitivity studies. First, a 1D radial flow with a semi-open boundary for verification is presented with the solution obtained by Oldenburg (2007). Sensitivities using multilayer models are considered to investigate the effects of gravity and heterogeneity on the conditions for the formation of the hydrate. The grid size is obtained using CMG Builder's recommended grid refinement, leading to enough refinement near the wellbore. It should be mentioned that a fine grid near the wellbore is required to properly capture the JT cooling and subsequent hydrate formation. An adaptive timestep is used. A fully implicit method was used for all simulations presented in this study because this formulation presented better convergence and stability when compared with the adaptive implicit method implemented in the commercial simulator considered in this work. Also, the minimum allowed residue tolerance was used to keep material balance errors at acceptable values. A small maximum timestep size was required for most cases to avoid excessive material balance errors and run failures.

Property and Parameters Survey and Validation

The first step is to validate the properties calculated with experimental data. This can help to be aware of any limitations imposed by these property models.

The K-values from Eq. 11 for both CO_2 and methane are shown at different temperatures in **Fig. 1**. The measured data used for calibration are water with zero salinity. While the latter assumption is unrealistic, it provides the worst-case scenario by making it more likely for hydrates to be formed. The calibration is provided by the CMG support team, and the parameters are presented in **Table 1**.

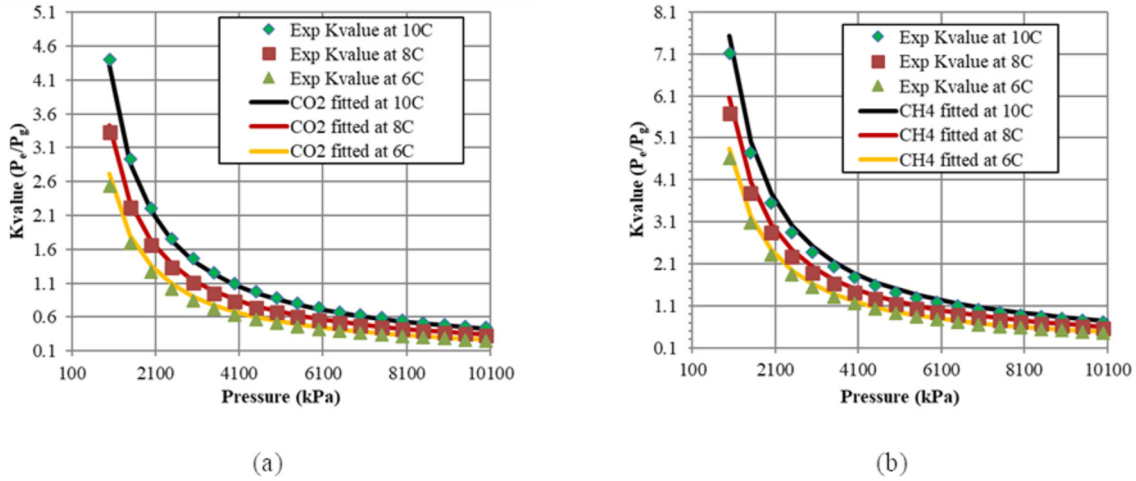

Fig. 1—Calibrated hydrate K-values, in which P_e is the hydrate equilibrium pressure at a given temperature and P_g is the gas pressure. (a) CO_2. (b) Methane.

Hydrate	r_1 (kPa)	r_2 (kPa$^{-1)}$	r_3	r_4 (°C)	r_5 (°C)
CO_2	1.7×10^9	0	0	−1485	−105.25
CH_4	1.6174×10^9	0	0	−1414.91	−105.25

Table 1—Calibrated coefficients for computing K-values performed by the CMG support team.

Table 2 summarizes the thermophysical properties of the CO_2 and CH_4 hydrates, obtained by laboratory experiments or computational chemistry simulations, provided by different authors.

References	Data Type	Values
Aya et al. (1997)	CO_2 hydrate density	1090–1110 kg/m^3 at 30 MPa
Takeya et al. (2016)	CO_2 hydrate density	1105 kg/m^3 at 268 K
Janicki et al. (2011)	CO_2 hydrate density	1106.805 kg/m^3
Sloan Jr and Koh (2007)	CH_4 hydrate density	900 kg/m^3
Janicki et al. (2011)	CH_4 hydrate density	919.94 kg/m^3
Mathews et al. (2020)	CO_2 hydrate heat capacity	148.86 J K^{-1} mol^{-1} (calculated with density functional theory)

Table 2—General hydrate data.

References	Data Type	Values
Ning et al. (2015)	CO_2 hydrate heat capacity	0–74.43 J K^{-1} mol^{-1} (molecular dynamics)
Handa (1986)	CH_4 hydrate heat capacity	107.7–257.6 J K^{-1} mol^{-1} from 85 K to 270 K
Nakagawa et al. (2008)	CH_4 hydrate heat capacity	164.38–197.26 J K^{-1} mol^{-1} – $c_p = 1.159T + 197.56$

Table 2 (continued)—General hydrate data.

A review of the published experimental and theoretical values of the other parameters in the hydrate kinetic model is summarized in **Table 3**. **Table 3** presents the activation energy for the hydrate dissolution obtained by different authors. Falenty et al. (2013) provided the activation energy for the CO_2 hydrate formation, but it was not included in **Table 3**, as their model was based on aqueous concentration rather than fugacity. Similarly, **Table 4** presents the reaction enthalpy obtained for CO_2 and CH_4 hydrates obtained by different authors.

References	Hydrate Type	Values	Type
Clarke and Bishnoi (2004)	CO_2	102.88 kJ/mol	Dissociation
Kim et al. (1987)	CH_4	78.151 ± 4.531 kJ/mol	Dissociation
Clarke and Bishnoi (2001)	CH_4	81 kJ/mol	Dissociation

Table 3—Hydrate activation energy.

References	Hydrate Type	Values (kJ/mol)	Type
Anderson (2003)	CO_2	63.6 ± 1.8 to 57.7 ± 1.8	Dissociation
Larson (1955)	CO_2	60.2	Dissociation
Bozzo et al. (1975)	CO_2	58.99 at 0°C, 58.16 at 10°C	Dissociation
Vlahakis et al. (1972)	CO_2	59.9	Dissociation
Long (1994)	CO_2	73	Dissociation
Kamath (1984)	CO_2	80.1	Dissociation
Yoon et al. (2003)	CO_2	57.66	Dissociation
Kang et al. (2001)	CO_2	65.22	Dissociation
Gjerstad (2019)	CO_2	–67.79 to –58.55	Formation
Janicki et al. (2011)	CO_2	65	Dissociation
Gjerstad (2019)	CH_4	–57.07 to –48.76	Formation
Anderson (2004)	CH_4	52.9	Dissociation
De Roo et al. (1983)	CH_4	67.85	Dissociation
Roberts et al. (1941)	CH_4	54.36	Dissociation
Deaton and Frost Jr (1946)	CH_4	55.12	Dissociation
McLeod and Campbell (1961)	CH_4	55.07	Dissociation
Marshall et al. (1964)	CH_4	53.41	Dissociation
Yoon et al. (2003)	CH_4	53.81	Dissociation
Glew (2002)	CH_4	55.36	Dissociation
Janicki et al. (2011)	CH_4	54	Dissociation

Table 4—Reaction enthalpy.

The values of the intrinsic reaction constant and hydrate-specific area are nontrivial. The first reason is that different models use different assumptions and do not apply to the model considered in this study. Another issue is that the hydrate-specific area is not constant and changes over time during the dissolution or growth of the hydrate particles, while the model considered here requires a constant value. To overcome this issue, the assumption from Hong and Pooladi-Darvish (2005) was considered by taking the hydrate particle diameter to be constant and equal to 16 μm. This results in a specific area of 3.75×10^5 m^{-1}. The intrinsic reaction constant and its product by the specific area obtained by different authors in the literature are presented in **Table 5**. We only consider the intrinsic reaction constants for the papers with a reaction rate based on fugacity or pressure difference (dominated by the gas phase). It is important to mention that values for methane hydrate formation are presented by Englezos et al. (1987) but are not presented here because their model was based on aqueous concentration.

Reference	Hydrate Type	K_d^0 (mol m^{-2}kPa^{-1}d^{-1})	$K_d^0 A_{hs}$ (mol m^{-3}kPa^{-1}d^{-1})	Type
Clarke and Bishnoi (2004)	CO_2	1.58×10^{16}	5.93×10^{21}	Dissociation
Kim et al. (1987)	CH_4	1.07×10^{13}	4.02×10^{18}	Dissociation
Clarke and Bishnoi (2001)	CH_4	3.11×10^{12}	1.17×10^{18}	Dissociation

Table 5—Intrinsic reaction constant.

The review of these data gives confidence in the values used in the simulations presented in this paper.

Finally, the gas viscosity parameters from Eq. 13 are $a_{CH_4} = 1.3 \times 10^{-4}$ cp and $b_{CH_4} = 0.7835$ for CH_4 and $a_{CO_2} = 1.048 \times 10^{-4}$ cp and $b_{CO_2} = 0.8784$ for CO_2. Again, the effect of pressure is not considered in Eq. 13. To evaluate the impact of pressure on viscosity, CO_2 and CH_4 gas viscosities are presented in **Fig. 2** against experimental data (NIST n.d.) for different pressures within the range considered in this work. The error in viscosity is not significant, with the maximum deviations being 6.55% and 6.60% for CH_4 and CO_2, respectively.

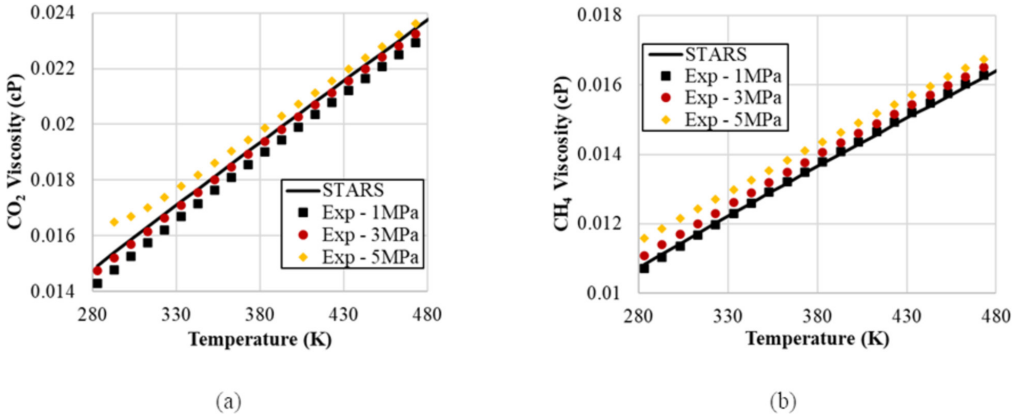

Fig. 2—Comparison of calculated gas viscosity for different temperature and pressure values (points are experimental data, and the black line is the STARS model). (a) CO_2. (b) CH_4.

The critical pressure, critical temperature, and acentric factors for CO_2 were 7.376 MPa, 31.05°C, and 0.225, respectively. Likewise, the critical pressure, critical temperature, and acentric factors for CH_4 were 4.600 MPa, −82.55°C, and 0.008, respectively.

Finally, a thorough comparison of the hydrate and thermal modeling between different simulators, including CMG STARS, is presented by Gaddipati (2008, 2014). However, JT cooling was not considered in these comparisons.

Results

Case 1: Verification with Oldenburg (2007). A 1D radial reservoir model was set up to verify the STARS capability of simulating the JT effect. The radial reservoir model has one injection well at the center that injects CO_2 into the reservoir and one producer at the outermost gridblock. The verification is performed by comparing the results from STARS with one case presented in Oldenburg (2007). The data considered for this case are presented in **Table 6**, where CO_2 is injected at a constant rate, while the CH_4 is produced through the outer boundary. A homogeneous permeability model is considered. Water is immobile, and the gas relative permeability is equal to

Parameter/Property	Value
Grid size ($N_r \times N_\theta \times N_z$)	100×1×1
Reservoir outer radius	1130 m
Reservoir thickness	50 m
Initial reservoir temperature	45°C
Injection temperature	45°C
Initial water saturation	0.2
Initial gas composition	100% CH_4
Porosity	0.3
Permeability	5 md
CO_2 injection rate	3 kg/s
CH_4 production rate	0.56 kg/s
Initial reservoir pressure	5 MPa

Table 6—Data for the verification case adapted from Oldenburg (2007).

its endpoint (1). Hydrates are not considered for this case. The maximum timestep size for this size (0.1 days) was considered. The final material balance error obtained with CMG STARS at the end of 1 year of simulation was 7.7×10^{-5}%. The number of gridblocks in the *r*-direction was 100, and a plot of the gridsize as a function of radius is presented in **Fig. 3**.

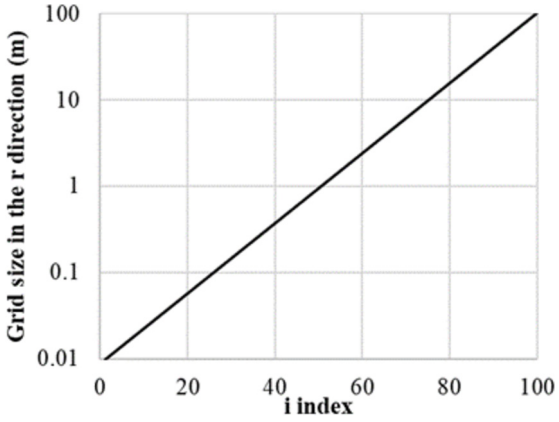

Fig. 3—Grid size in the *r*-direction vs. gridblock index for Case 1.

Fig. 4 compares reservoir temperature, pressure, and the CO_2 overall composition profiles with those obtained by Oldenburg using TOUGH2 with similar results. In this figure, the distance from the well (*x*-axis) represents the radial distance from the injector well. While the results are similar, some differences can be observed. It is hard to exactly point out the reason for the differences since both simulators are black boxes with very limited details of the models and methods of solutions. A higher cooling can be observed in STARS for all the time in **Fig. 4a**. The causes for this could be related to different well models used, the different models used to compute departure enthalpy, different grid sizes, or even certain properties not presented by Oldenburg (2007) such as viscosity and heat capacity for the fluids. It should also be noted that CMG STARS does not consider binary interaction coefficients for computing the gas density, which can cause slight changes in the density of the CO_2-CH_4 mixture in the mixing zone. The differences in the CO_2 mole fraction profile **(Fig. 4c)** are

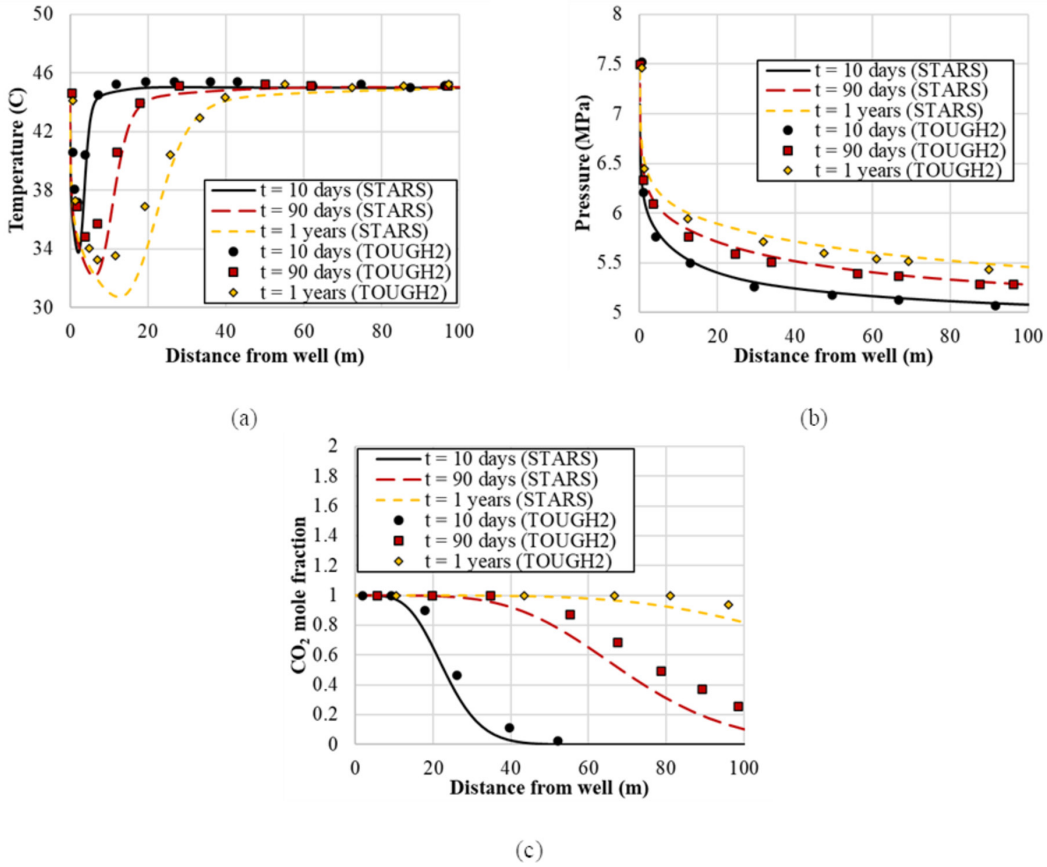

Fig. 4—Comparison of profiles for Case 1 with the markers representing the data from Oldenburg (2007) (TOUGH2) and the lines representing the results from this study using the commercial simulator (STARS). (a) Temperature. (b) Pressure. (c) CO_2 overall mole fraction.

most likely a consequence of the higher cooling obtained with STARS. The higher cooling leads to a region with lower density CO_2, which will result in a slightly apparent delay of the CO_2 front.

The drop in temperature observed in **Fig. 4a** is caused by the JT cooling and can also be observed in other works in the literature (Mathias et al. 2010; Creusen 2018; Aghajanloo et al. 2024; Chesnokov et al. 2024; Yamada et al. 2024). It should be mentioned that unlike in radial flow, the effects of JT cooling in 1D linear flows are considerably less as noted in other works such as Singh et al. (2020) who point out the possibility of using isothermal simulators for hydrate modeling. However, one should keep in mind that the pressure and velocity distributions near vertical wells are better described by radial (or 2D) flow rather than a 1D linear flow.

Case 2: Hydrate Study in a Homogeneous Reservoir. This case considers an infinite boundary homogeneous reservoir modeled with a 1D radial grid. The case considers the same grid as the previous case and is presented in **Fig. 2**. Pore volume multipliers are used in the outermost gridblock to emulate an infinite reservoir. The reservoir model has one injection well at the center that injects CO_2 into the reservoir. No producer wells are considered for this case. A sensitivity study was performed on this model to understand the impact of heat exchange on surrounding formations and permeability reduction. Reservoir temperature, pressure, CO_2 hydrate concentration, gas saturation, and porosity profiles are plotted to display the effects of heat exchange and permeability reduction. Unlike the previous case, there is no CH_4 production and pore volume multipliers are used in the external boundary to simulate an infinite boundary reservoir. **Table 7** presents the reservoir data for this case. The heat exchange to underburden and overburden formations is computed with the boundary condition proposed by Vinsome and Westerveld (1980). The maximum timestep size used for this case was 0.01 days. Larger timestep sizes lead to run problems and severe material balance errors. Material balance errors were less than 10^{-4}%.

Parameter/Property	Value
Grid size ($N_r \times N_\theta \times N_z$)	100×1×1
Reservoir outer radius	1130 m
Reservoir thickness	50 m
Reservoir initial temperature	45°C
Injection temperature	10°C
Water initial saturation	0.2
Porosity	0.3
Permeability	20 md
Gas initial composition	100% CH_4
CO_2 injection rate	0.0946 MMTA (3 kg/s)
Reservoir initial pressure	3 MPa
k_v/k_h	0.1
Rock heat capacity	1000 kJ/(m^3 °C)
Rock heat conductivity	217 kJ/(m °C d)
Heat exchange to the surroundings	Sensitivity
Base/Caprock heat capacity	1000 J/(kg °C)
Base/Caprock heat conductivity	2.51 W/(m °C)
Permeability reduction	Sensitivity

Table 7—Model data, reservoir, and fluid parameters for Case 2.

Hydrate parameters used for Case 2 are based on the data from the literature presented in the previous section. **Table 8** shows all hydrate parameters used for Case 2. These hydrate parameters are also used in the next sensitivity study named Case 3. Furthermore, the formation of hydrate is an exothermic process, thus releasing heat, while the dissociation is an endothermic process, thus taking heat from the surroundings. Finally, the formation of ice is modeled in STARS with latent heat (phase equilibrium) rather than a kinetics-like approach.

Parameter/Property	CO_2	CH_4	Ice
Density (kg/m^3)	1100	919.7	~916.89
Heat capacity (J mol^{-1} °C^{-1})	148.86	191.2	~37.12
Formation enthalpy (kJ/mol)	60	55	–
Dissociation enthalpy (kJ/mol)	–60	–55	–
Formation activation energy (kJ/mol)	102	81	–
Dissociation activation energy (kJ/mol)	102	81	–
Formation reaction constant product, $\left(K_d^0 A_{hs}\right)$ (mol m^{-3} kPa^{-1} d^{-1})	4.02×10^{18}	5.93×10^{21}	–

Table 8—Hydrate parameters for Cases 2 and 3.

Parameter/Property	CO_2	CH_4	Ice
Dissociation reaction constant product, $\left(K_d^0 A_{hs}\right)$ (mol m^{-3} kPa^{-1} d^{-1})	4.02×10^{18}	5.93×10^{21}	–
Formation reaction frequency, $\left(\frac{K_d^0 A_{hs}}{\rho_w \rho_h}\right)$	3.65×10^{12}	6.45×10^{15}	–
Dissociation reaction frequency, $\left(\frac{K_d^0 A_{hs}}{\rho_w \rho_h}\right)$	3.65×10^{12}	6.45×10^{15}	–
Latent heat of fusion (kJ/mol)	–	–-	6.0

Table 8 (continued)—Hydrate parameters for Cases 2 and 3.

First, a sensitivity for the heat exchange (h_l) with the overburden and underburden formations is presented. **Fig. 5** presents a comparison of results obtained without and with heat exchange to the surrounding formations. **Fig. 5a** presents the near-wellbore temperature profiles at 10 days, 30 days, and 90 days of simulation. The heat exchange with surrounding formations creates a slight increase in temperature. As the time increases from 10 days to 90 days, one can observe a larger separation between the corresponding profiles. The temperature increase does not impact the pressure profiles in the near-wellbore region **(Fig. 5b)**. In addition, there is a plateau in the temperature profile at 0°C after 90 days of simulation. This is caused by the formation of ice and how this is modeled by the numerical simulator. In STARS, ice is formed in a similar fashion to a pure component phase transition with a freezing temperature and latent heat. Therefore, temperature can only go below freezing temperature after all water is converted into ice or hydrates. CO_2 hydrates were formed in both scenarios with a decrease in the amount of hydrates observed when heat exchange is considered **(Fig. 4c)**. The porosity profiles **(Fig. 4d)** follow a similar behavior to the CO_2 hydrate concentration profiles. It can be observed from the temperature, CO_2 hydrate concentration, and porosity profiles that the effect of heat exchange with surrounding formations seems to intensify over time and cannot prevent hydrates from forming early in time. This would suggest that hydrates could be prevented by the heat exchange if hydrates were to be formed late in time.

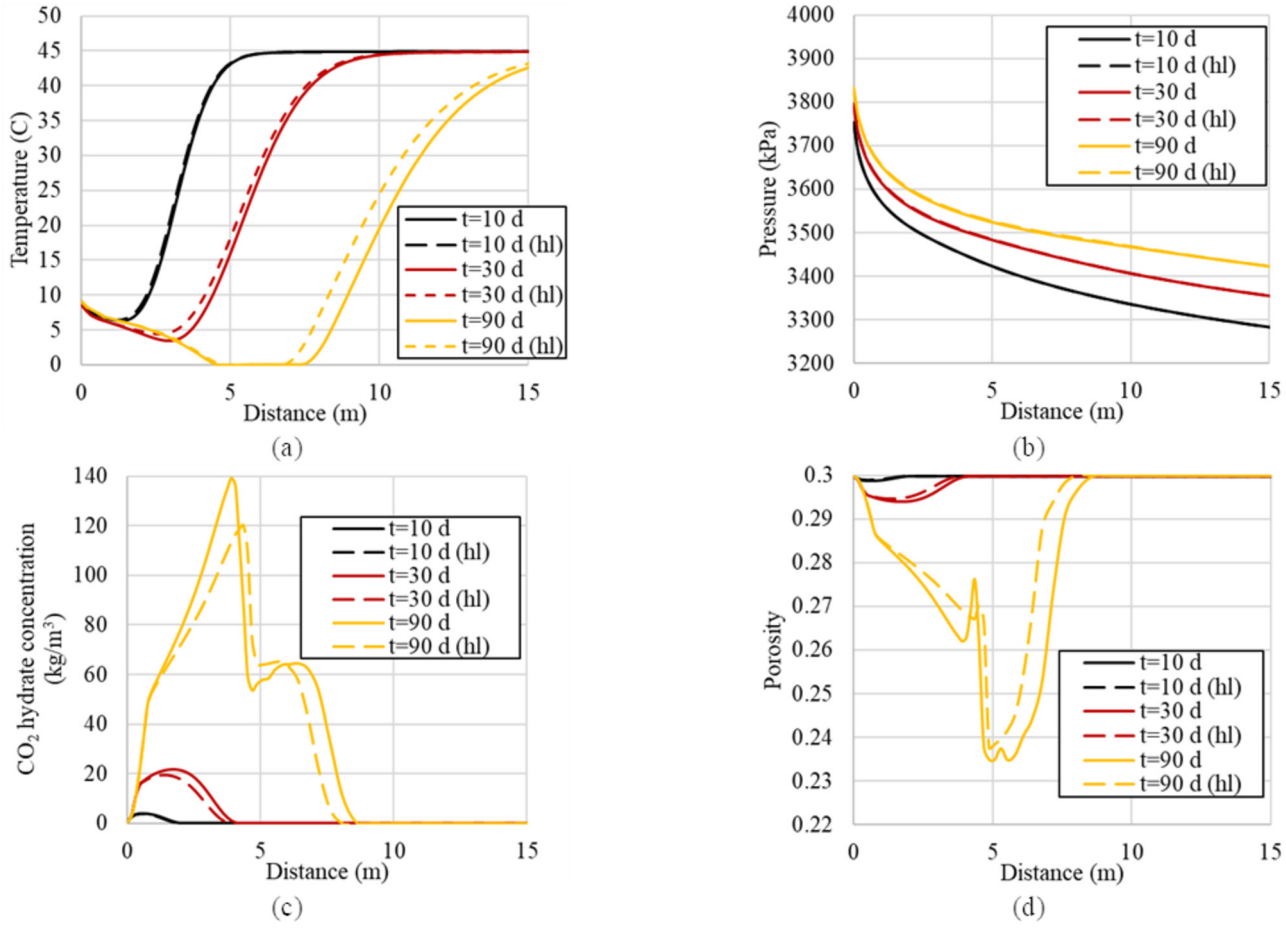

Fig. 5—Comparison of results for Case 2 with (dashed line) and without (solid line) heat exchange to the surrounding formations. (a) Temperature. (b) Pressure. (c) CO_2 hydrate concentration. (d) Porosity.

Next, a sensitivity to the permeability reduction is presented. The results of two simulations with and without permeability reduction are compared and different profiles are presented in **Fig. 6**. Both scenarios model heat exchange as presented before. The permeability reduction exponent (C_k) for the case with permeability reduction was two, where an input value of zero results in no permeability reduction. The near-wellbore temperature profiles are presented in **Fig. 6a** for 10 days, 30 days, and 90 days of simulation. More cooling can

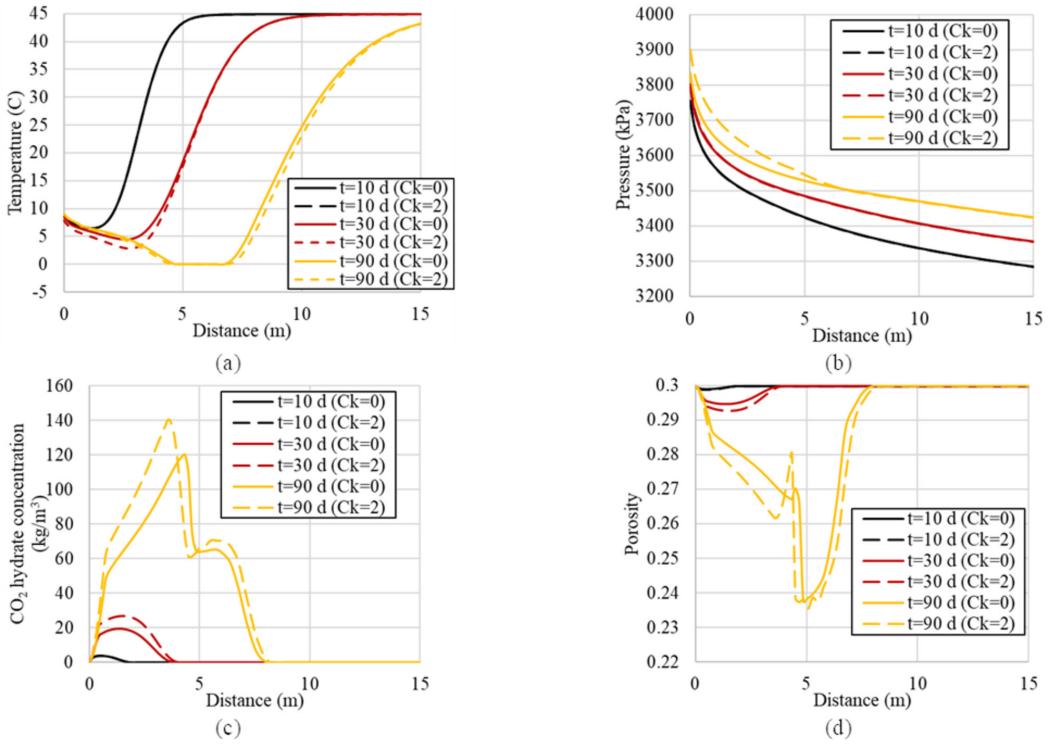

Fig. 6—Comparison of results for Case 2 with (dashed line) and without (solid line) modeling heat transfers from the surrounding formations. (a) Temperature. (b) Pressure. (c) CO_2 hydrate concentration. (d) Porosity.

be observed when permeability reduction is considered. As permeability reduces, the JT cooling increases because of the larger pressure drawdown. The increase in pressure can be observed in **Fig. 6b**, especially at 90 days. As seen in **Fig. 6c**, CO_2 hydrates formed in the region with higher pressure values. The amount of CO_2 hydrates formed is also larger in the case with permeability reduction because of more significant JT cooling. Porosity profiles of the reservoir in **Fig. 6d** follow a trend similar to the CO_2 hydrate concentration profiles in **Fig. 6c**. From **Fig. 6a through 6d**, we can see that the effect of permeability reduction becomes more significant with time as more hydrate is formed. One important observation on the porosity profile **(Fig. 5d)** is the magnitude of porosity reduction when CO_2 hydrates are formed. It is clearly seen in **Fig. 6d** that the maximum porosity reduction is around 20%. This reduction is in agreement with the amount of water originally in place. Hydrates and ice are only formed while liquid water is present in the porous media. Therefore, more water could lead to more porosity and permeability reduction.

A sensitivity of the injectivity to the permeability reduction is presented in **Fig. 7**. Here, the case without permeability reduction and without heat exchange is also included. Also, a case with a permeability reduction exponent (C_k) of 5 is considered. It can be observed that the injectivity does reduce for all cases. However, its reduction is more significant when permeability reduction is included as it would be expected. The injectivity reduces by 44% with a value of $C_k = 5$. One should note that such a value is not unusual in actual field applications as Uddin et al. (2008a) used a value of $C_k = 10$, based on experimental data. It can also be observed that the impact of heat exchange on the injectivity is negligible.

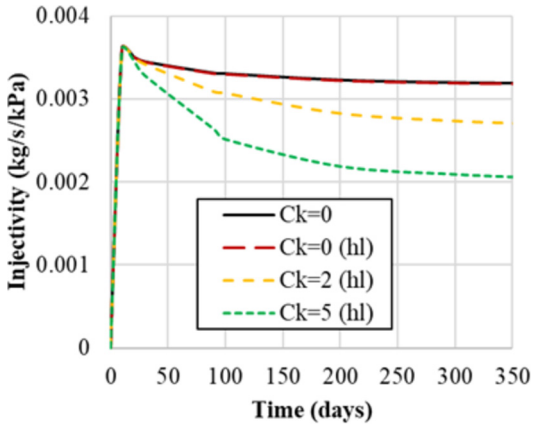

Fig. 7—Comparison of the injectivity over time for different scenarios. "Ck = 0" denotes no permeability reduction, while "hl" indicates that heat exchange is considered.

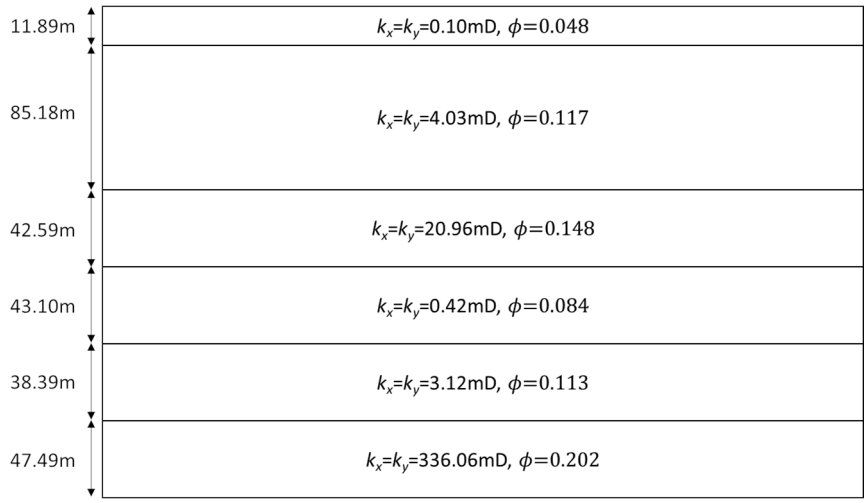

Fig. 8—Reservoir layer properties for Case 3.

Parameter/Property	Value	Sensitivity
Reservoir type	Radial infinite	–
Grid size (N_r×N_θ×N_z)	100×1×6	
Reservoir initial temperature	135°C	–
Injection temperature	10°C	–
Initial water saturation	0.2	0.15 and 0.3
Gas initial composition	100% CH_4	–
CO_2 injection rate	1 MMTA (~31.71 kg/s)	0.5 and 2 MMTA
Initial reservoir pressure	2.5 MPa	1 and 4 MPa
k_v/k_h	0.1	0.5 and 1
Rock heat capacity	2600 kJ/(m^3 °C)	–
Heat conductivity	217 kJ/(m °C d)	–
Heat exchange to the surroundings	None	Include under and overburden
Capillary pressure	Not considered	*J*-function **(Fig. 9)**
Interfacial tension	0.03 N/m	–
Permeability reduction (C_k)	0	2

Table 9—Model data and sensitivity analysis parameter for Case 3.

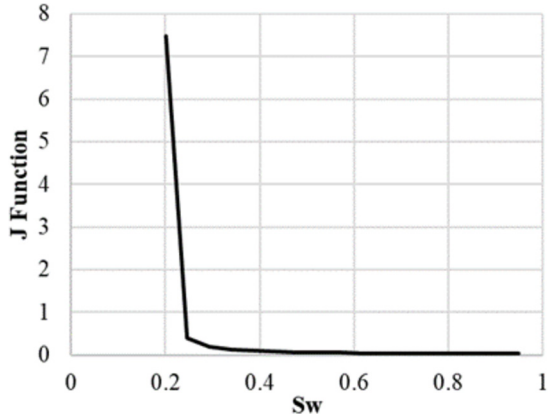

Fig. 9—Leverett J function vs water saturation (S_w) considered for Case 3.

Case 3: Layered Radial Reservoir. A reservoir model is built considering the upscaled data of a well log. A sensitivity analysis is performed to understand the different effects of the CO_2 injection in this formation. The reservoir model considers six layers and is assumed to be radially infinite using a pore volume multiplier at the outer boundary control volumes. A description of the reservoir model (including thickness, permeability, and porosity for each layer) is presented in **Fig. 8**. The depth at the top of the reservoir is 2893.61 m. The model data and sensitivity parameters are presented in **Table 9**. The parameters considered for sensitivity were the initial reservoir pressure, initial water saturation, injection rate, and ratio between the horizontal to vertical permeability. The base model does not consider the effects of capillary pressure, permeability reduction, and heat exchange to surrounding formation and these are included as sensitivity scenarios. For the scenario with capillary pressure, the *J*-function presented in **Fig. 9** is used. The hydrate kinetic model parameters are presented in **Table 8**. The maximum timestep size used for this case was 0.003 days. Larger timestep sizes lead to run problems and severe material balance errors. Material balance errors were less than 10^{-4}%.

The near-wellbore temperature field for the base case at 1 year of simulation is presented in **Fig. 10a**. The temperature changes are observed to be more significant in the higher-permeability layers, with most of the temperature variation in the sixth layer (k_h = 336.06 md) (deepest layer) followed by the third layer (k_h = 20.96 md). This is a consequence of the higher flow rate through these layers, which can be seen from the CO_2 front presented in **Fig. 10d**. Also, as CO_2 is injected into the formation, the water will slowly vaporize into the gas phase, causing a dry-out effect. In this case, this effect can be observed near the wellbore in **Fig. 10b**, with water saturation being reduced to zero near the wellbore. A significant reduction in water saturation can also be observed a bit farther from the well, which coincides with a reduction in porosity **(Fig. 10c)** that is caused by the formation of ice and hydrates combined. While water dry-out could help mitigate the formation of ice and hydrates by reducing water content, it can be observed that the water-drying front moves slower than the temperature-cooling front. Therefore, hydrates and ice still form for this case. The temperature profiles for the sixth layer at 10 days, 90 days, and 1 year of simulation are presented in **Fig. 11**, from which can be observed no significant difference from what would be observed from a 1D radial case such as the one presented in Case 2. However, a higher temperature near the wellbore can be observed at the sixth layer (about 12°C) due to the higher pressure in that layer. On the other hand, the minimum temperature observed within the reservoir is as low as 0°C after a year of injection with the formation of CO_2 hydrates and ice. The maximum distance of the temperature front from the wellbore after 1 year was 114.85 m. It should also be noted that the *x*-axis in **Fig. 10** refers to the radial distance from the

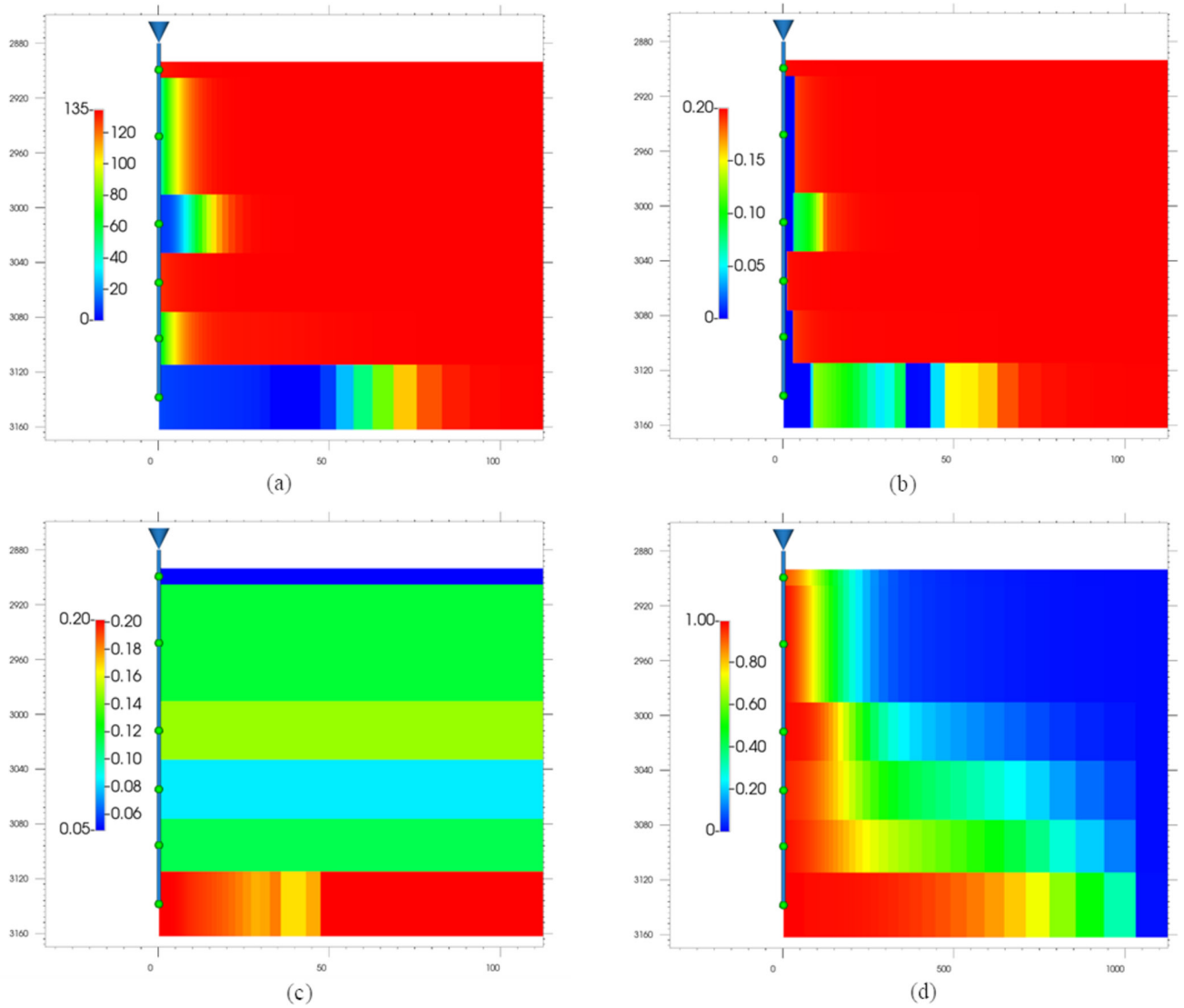

Fig. 10—Cross-section (radius vs. depth) plots at 1 year of simulation for Case 3 base scenario. (a) Temperature in °C. (b) Water saturation. (c) Porosity. (d) CO_2 mole fraction in the gas phase.

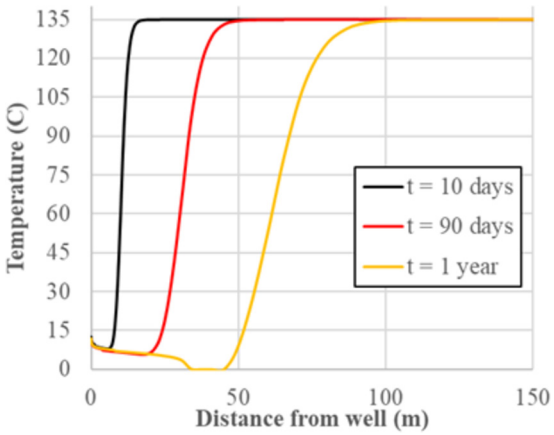

Fig. 11—Temperature profiles (distance from the well) vs. time for the sixth layer from the base scenario for Case 3.

injector well, and velocity decreases radially. This can mislead one into believing that the rate being injected into the low permeability layers is comparable to the injection rate into the high-permeability layers (bottom one). In fact, more than 90% of the CO_2 is injected into the high-permeability layer. This can be observed in a plot of the mass injection rate in each layer **(Fig. 12)**.

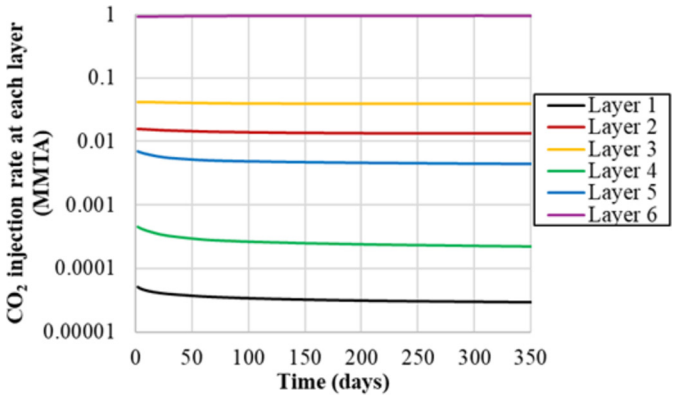

Fig. 12—Injection rate at each well's segment for Case 3 base scenario. Layers are numbered from shallowest (Layer 1) to deepest (Layer 6).

Most of the sensitivity scenarios considered resulted in the formation of hydrates as presented in **Table 10**. The only scenarios with no hydrate formation were the ones with lower injection rates and when heat exchange was considered.

Parameter/Property	Lower Value	Higher Value
CO_2 injection rate	0.5 MMTA	2 MMTA
Reservoir initial pressure	1 MPa	4 MPa
k_v/k_h	0.05	1
Water saturation (S_w)	0.15	0.3
Capillary pressure (P_c)	–	Included
Heat exchange to surrounding (HE)	–	Included
Permeability reduction (C_k)	–	2

Table 10—Hydrate risk sensitivity for Case 3 after 1 year of CO_2 injection at 10°C (shaded cells represent the cases in which hydrate formed).

While most cases present the formation of hydrates and even ice, the movement and behavior of the temperature over time varies among them. To summarize such differences, a tornado plot of changes in the minimum temperature is presented in **Fig. 13** for 30 days, 90 days, 180 days, and 365 days of simulation. It is possible to observe that the minimum temperature of the base case decreases over time and eventually reaches the freezing temperature, which was also observed in **Fig. 12**. The inclusion of heat exchange mitigates the decrease in initial temperature over time. In fact, the minimum temperature stops decreasing after some time when heat exchange is considered (the minimum temperature at 180 days and 365 days is very close). On the other hand, permeability reduction further reduced the JT cooling leading to freezing temperatures observed sooner than the base case scenario. Initial water saturation also had some impact on

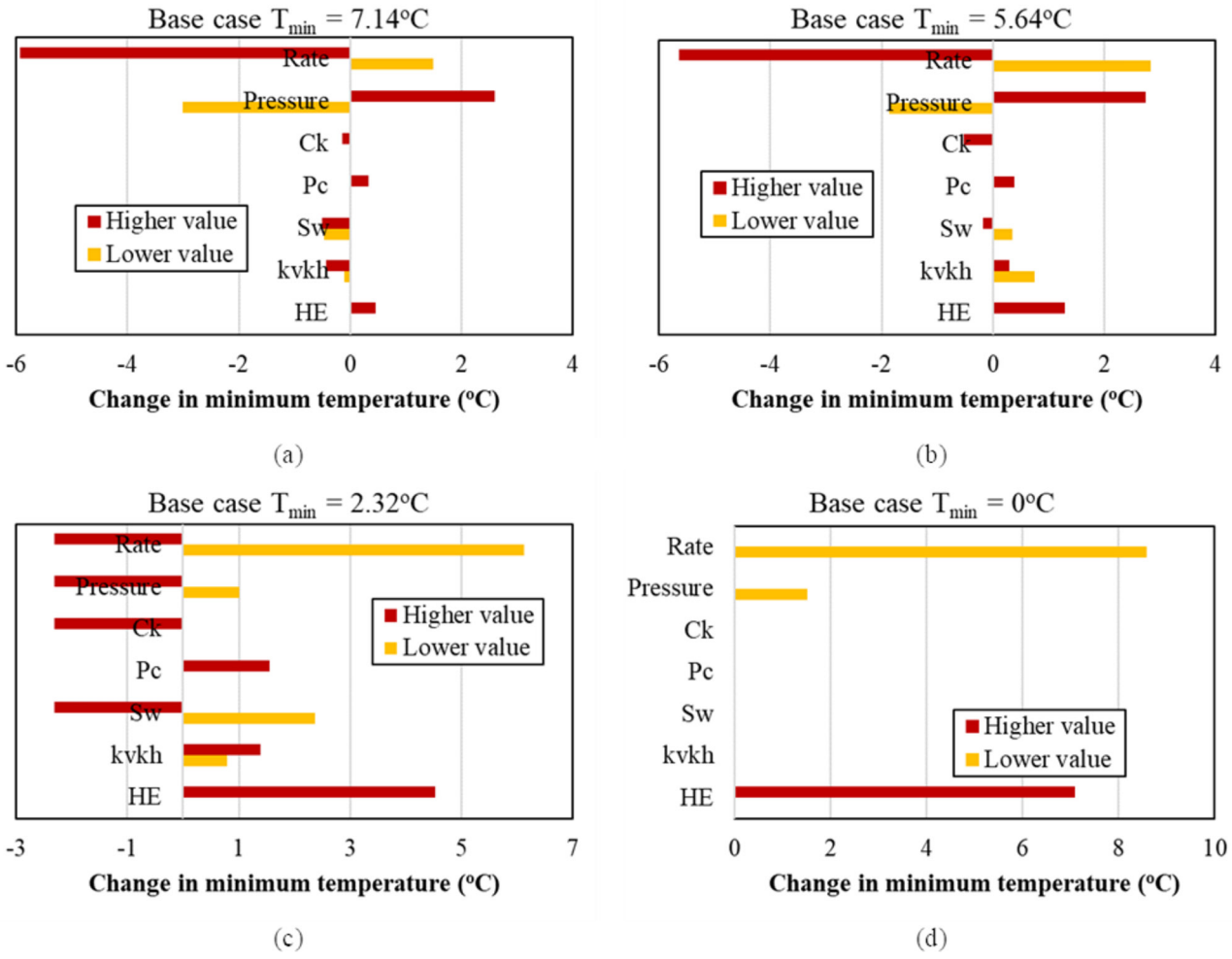

Fig. 13—Tornado plots for the changes in minimum temperature with respect to the base scenario for Case 3 (see Table 10). (a) 30 days, (b) 90 days, (c) 180 days, and (d) 365 days.

the temperature behavior. It was observed that higher water saturation resulted in lower temperatures while lower water saturation led to higher temperatures. The increase in water content leads can lead to more hydrate formation when CO_2 is injected. The first reason is that more water is available to be converted into hydrates. The second reason is that the CO_2 dry-out effect becomes less relevant as the water content increases and hydrates can form. Another reason observed in the simulations is the expansion of CO_2 when hydrates are formed, which leads to more JT cooling. It is important to mention that the dry-out effect was not observed to prevent hydrates in any case. The impact of k_v/k_h is small with a maximum difference of 1°C. However, this could be due to the huge contrast between layers. It is also important to note that CO_2 flows favorably in the bottom layer due to methane's lower density, water being immobile, and the considerably higher permeability of the bottom layer. The inclusion of capillary pressure was observed to increase temperature only slightly. The

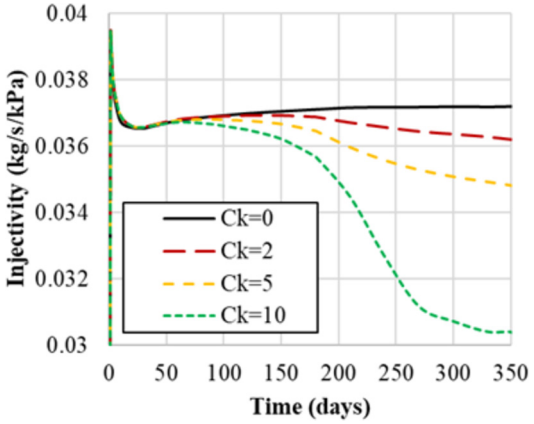

Fig. 14—Sensitivity of the injectivity to permeability reduction exponent parameter (C_k). "Ck = 0" denotes no permeability reduction.

initial reservoir pressure had a high impact on the temperature behavior. An increase in the initial pressure leads to a decrease in the JT cooling. However, it also leads to an increase in the hydrate equilibrium temperature and a further decrease in temperature once hydrates start forming. On the other hand, a lower initial pressure results in more JT cooling and a lower hydrate equilibrium temperature, which can lead to hydrates forming at a later time, consistent with the behavior observed in **Fig. 12**. At 30 days and 90 days of simulation, the amount of CO_2 hydrates is negligible for both the 1-MPa and 4-MPa cases. At 180 days, a moderate amount of hydrates is present for the 4-MPa scenario, while the amount of hydrates is still negligible for the 1-MPa scenario, which results in the inversion of the trend. At 365 days, both cases have a moderate amount of hydrates, but the 4-MPa scenario has a much higher amount. Finally, the parameter with the highest impact was the injection rate. As expected, increasing the injection rate results in a higher-pressure drawdown and more JT cooling, while decreasing the injection rate results in lower pressure drawdown and less JT cooling.

A comparison of the injectivity for different values of permeability reduction exponent (C_k) is presented in **Fig. 14**. This figure considers the base scenario ($C_k = 0$) and the scenario with $C_k = 2$. Scenarios with $C_k = 5$ and $C_k = 10$ were also included. From this figure, it is possible to observe that the injectivity is the same for about 50 days when hydrates start forming and the injectivity starts behaving differently for each scenario. It is possible to observe a reduction of about 21% in the injectivity for the case with the highest permeability reduction.

Conclusions

This paper provides insights into the fluid and reservoir conditions under which CO_2 and water can transition into hydrates and ice in the reservoir near the injection well. The formation of hydrate can cause severe permeability and injectivity loss, which is detrimental to the CCS project goals. The results emphasize the importance of CO_2 injection conditions (rate, pressure, and temperature) and reservoir properties (initial pressure, water saturation, capillary pressure, vertical-to-horizontal permeability ratio, and heat exchange) to consider in the selection of storage sites to minimize operational risk. Common hydrate mitigation strategies are costly (i.e., heating CO_2 at the wellhead or injecting thermodynamic chemical inhibitors).

A summary of the results is presented as follows:

- The water dry-out zone was not too deep into the reservoir to prevent hydrate formation since the cold temperature front moved ahead of the dry-out zone.
- Heat exchange with the underburden and overburden rocks mitigates hydrate formation in the multilayer case with an increase in the lowest temperature.
- The effect of the initial reservoir pressure is complex. An increase in pressure results in less JT cooling initially but leads to more hydrates and lower temperatures at later times. The opposite is observed when the initial reservoir pressure is reduced.
- The minimum temperature in the reservoir was not sensitive to the ratio of vertical-to-horizontal permeabilities.
- Initial water saturation impacts the lowest temperature at later times. More hydrates and JT cooling are observed at higher water saturations.
- Permeability reduction amplified the JT cooling and increased the amount of hydrates. However, no plugging is observed by either hydrates or ice in the sensitivity simulations.
- The injection rate has the most impact on the JT cooling and formation of hydrates. The increase in injection rate requires higher bottomhole pressure, which further increases the JT cooling effect.
- The reduction in injectivity was less than 44% and 21% for Cases 2 and 3, respectively.

Despite the relatively low reduction in injectivity observed by the hydrates, care should still be exercised. Other phenomena not investigated in this work such as water backflow and salt precipitation may intensify the reduction in injectivity. Such phenomena will be the subject of future investigations.

Nomenclature

a = constants or fitting parameters
A = surface area, m^2
b = constants or fitting parameters
c = concentration, mol m^{-3}
c_p = specific heat capacity, J mol^{-1} K^{-1}
E = activation energy, kJ mol^{-1}
f = fugacity, Pa
H = enthalpy, kJ mol^{-1}
I = injectivity, kg $s^{-1}kPa^{-1}$
K = equilibrium ratio
k = permeability, md
M = molecular weight, g mol^{-1}
m = injection mass rate, kg/s
n = number of moles, mol
P = pressure, Pa
r = constants or fitting parameters
R = gas constant, J mol^{-1} K^{-1}
S = saturation
t = time, seconds
T = temperature, K
V = volume, m^3
x = liquid mole fraction
μ = viscosity, cp
μ_{JT} = Joule-Thomson coefficient
ρ = density, kg m^{-3}
ϕ = porosity
ω = mixture acentric factor

Subscript

0 = reference condition
bh = bottomhole
c = critical condition
g = gas phase
h = hydrate phase
i = ith component
j = jth component
R = reservoir
s = specific hydrate surface area
w = water phase

Superscript

0 = simple fluid departure enthalpy
$*$ = fugacity of component h in the gas-hydrate equilibrium
(r) = reference fluid
depart = enthalpy departure
ideal = ideal enthalpy
g = fugacity of component h in the gas phase

Acknowledgments

The authors acknowledge the sponsors of the RS-JIP from the Center for Subsurface Energy and the Environment at The University of Texas at Austin and Shell for the financial support of this work. The authors also thank the Computer Modeling Group for providing access to the CMG-STARS. Rouhi Farajzadeh would like to acknowledge Shell Global Solutions International for their permission to publish this work.

References

Aghajanloo, M., Yan, L., Berg, S. et al. 2024. Impact of CO_2 Hydrates on Injectivity during CO_2 Storage in Depleted Gas Fields: A Literature Review. *Gas Sci Eng* **123**: 205250. https://doi.org/10.1016/j.jgsce.2024.205250.

Ahmad, S., Li, Y., Li, X. et al. 2019. Numerical Analysis of CO_2 Hydrate Growth in a Depleted Natural Gas Hydrate Formation with Free Water. *Greenhouse Gases* **9** (6): 1181–1201. https://doi.org/10.1002/ghg.1924.

Al Hagrey, S. A., Köhn, D., and Rabbel, W. 2014. Geophysical Assessments of Renewable Gas Energy Compressed in Geologic Pore Storage Reservoirs. *Springerplus* **3** (1). https://doi.org/10.1186/2193-1801-3-267.

Al Maqbali, Q., Hussain, S., Mask, G. et al. 2023. Numerical Simulation of In-Situ CO_2 Mineralization in Mafic Basaltic Formations in Southwest Oklahoma. Paper presented at the SPE Oklahoma City Oil and Gas Symposium, Oklahoma City, Oklahoma, USA, 17−19 April. https://doi.org/10.2118/213084-MS.

Anderson, G. K. 2003. Enthalpy of Dissociation and Hydration Number of Carbon Dioxide Hydrate from the Clapeyron Equation. *J Chem Thermodyn* **35** (7): 1171–1183. https://doi.org/10.1016/S0021-9614(03)00093-4.

Anderson, G. K. 2004. Enthalpy of Dissociation and Hydration Number of Methane Hydrate from the Clapeyron Equation. *J Chem Thermodyn* **36** (12): 1119–1127. https://doi.org/10.1016/j.jct.2004.07.005.

Aya, I., Yamane, K., and Nariai, H. 1997. Solubility of CO_2 and Density of CO_2 Hydrate at 30 MPa. *Energy* **22** (2–3): 263–271. https://doi.org/10.1016/S0360-5442(96)00093-X.

Bouzalakos, S. and Mercedes, M. 2010. Overview of Carbon Dioxide (CO_2) Capture and Storage Technology. In *Developments and Innovation in Carbon Dioxide (CO2) Capture and Storage Technology*, ed. M. M. Maroto-Valer, Chap. 1, 1–24. New York: Woodhead Publishing.

Bozzo, A. T., Hsiao-Sheng, C., Kass, J. R. et al. 1975. The Properties of the Hydrates of Chlorine and Carbon Dioxide. *Desalination* **16** (3): 303–320. https://doi.org/10.1016/S0011-9164(00)88004-2.

Burke, L. 2011. Carbon Dioxide Fluid-Flow Modeling and Injectivity Calculations. Scientific Investigations Report No. 2011-5083. U.S. Geological Survey, Reston, Virginia, USA.

Chesnokov, C., Farajzadeh, R., Prempeh, K. O. K. et al. 2024. Analytical Model for Joule-Thomson Cooling under Heat Exchange during CO_2 Storage. *Adv Water Resour* **190**: 104758. https://doi.org/10.1016/j.advwatres.2024.104758.

Clarke, M. and Bishnoi, PR. 2001. Determination of the Activation Energy and Intrinsic Rate Constant of Methane Gas Hydrate Decomposition. *Can J Chem Eng* **79** (1): 143–147. https://doi.org/10.1002/cjce.5450790122.

Clarke, M. A. and Bishnoi, P. R. 2004. Determination of the Intrinsic Rate Constant and Activation Energy of CO_2 Gas Hydrate Decomposition Using In-Situ Particle Size Analysis. *Chem Eng Sci* **59** (14): 2983–2993. https://doi.org/10.1016/j.ces.2004.04.030.

Coelho, F. M. C., Sepehrnoori, K., and Ezekoye, O. A. 2021a. A Coupled Hydrate and Compositional Wellbore Simulator: Understanding Hydrate Inhibition from Associated Brines in Oil and Gas Production. *SPE Prod & Oper* **36** (4): 858–872. https://doi.org/10.2118/206716-PA.

Coelho, F. M. C., Sepehrnoori, K., and Ezekoye, O. A. 2021b. Coupled Geochemical and Compositional Wellbore Simulators: A Case Study on Scaling Tendencies under Water Evaporation and CO2 Dissolution. *J Pet Sci Eng* **202**: 108569. https://doi.org/10.1016/j.petrol.2021.108569.

Cook, J., Oreskes, N., Doran, P. T. et al. 2016. Consensus on Consensus: A Synthesis of Consensus Estimates on Human-Caused Global Warming. *Environ Res Lett* **11** (4): 048002. https://doi.org/10.1088/1748-9326/11/4/048002.

Creusen, M. C. M. 2018. *Near Wellbore Effects Induced by CO_2 Injection and the Influence on Injectivity in Depleted Gas Reservoirs*. Master thesis, Delft University of Technology, Delft, Netherlands.

de Kok, J. 2024. Monitoring Injectivity for CO_2 Injection in Depleted Gas Reservoirs. Paper presented at the SPE Europe Energy Conference and Exhibition, Turin, Italy, 26−28 June. https://doi.org/10.2118/220119-MS.

De Roo, J. L., Peters, C. J., Lichtenthaler, R. N. et al. 1983. Occurrence of Methane Hydrate in Saturated and Unsaturated Solutions of Sodium Chloride and Water in Dependence of Temperature and Pressure. *AIChE J* **29** (4): 651–657. https://doi.org/10.1002/aic.690290420.

Deaton, W. M. and Frost Jr, E. M. 1946. Gas Hydrates and Their Relation to the Operation of Natural-Gas Pipe Lines. Report No.: BM-Mon-8. Helium Research Center, Bureau of Mines, Amarillo, TX, USA.

Englezos, P., Kalogerakis, N., Dholabhai, P. D. et al. 1987. Kinetics of Formation of Methane and Ethane Gas Hydrates. *Chem Eng Sci* **42** (11): 2647–2658. https://doi.org/10.1016/0009-2509(87)87015-X.

Falenty, A., Salamatin, A. N., and Kuhs, W. F. 2013. Kinetics of CO_2 -Hydrate Formation from Ice Powders: Data Summary and Modeling Extended to Low Temperatures. *J Phys Chem C* **117** (16): 8443–8457. https://doi.org/10.1021/jp310972b.

Gaddipati, M. 2008. *Code Comparison of Methane Hydrate Reservoir Simulators Using CMG STARS*. Master thesis, West Virginia University, Morgantown, West Virginia, USA.

Gaddipati, M. 2014. *Reservoirs Modeling of Gas Hydrate Deposits in North Slope of Alaska and Gulf of Mexico*. PhD dissertation, West Virginia University, Morgantown, West Virginia, USA.

Gauteplass, J., Almenningen, S., Barth, T. et al. 2020. Hydrate Plugging and Flow Remediation during CO_2 Injection in Sediments. *Energies* **13** (17): 4511. https://doi.org/10.3390/en13174511.

Gauteplass, J., Almenningen, S., Ersland, G. et al. 2018. Hydrate Seal Formation during Laboratory CO_2 Injection in a Cold Aquifer. *Int J Greenh Gas Control* **78**: 21–26. https://doi.org/10.1016/j.ijggc.2018.07.017.

Gjerstad, PB. 2019. *Enthalpies of CH_4 and CO_2 Hydrate Formation and Dissociation Using Residual Thermodynamics*. Master's thesis, University of Bergen, Bergen, Norway.

Glew, D. N. 2002. Aqueous Nonelectrolyte Solutions. Part XVIII. Equilibrium Pressures of Two Methane Hydrates with Water. Formulae and Dissociation Thermo -Dynamic Functions for the Structures I and II Methane Hydrates. *Can J Chem* **80** (4): 418–439. https://doi.org/10.1139/v02-017.

Han, W. S., Stillman, G. A., Lu, M. et al. 2010. Evaluation of Potential Nonisothermal Processes and Heat Transport during CO_2 Sequestration. *J Geophys Res* **115** (B7). https://doi.org/10.1029/2009JB006745.

Handa, Y. P. 1986. Compositions, Enthalpies of Dissociation, and Heat Capacities in the Range 85 to 270 K for Clathrate Hydrates of Methane, Ethane, and Propane, and Enthalpy of Dissociation of Isobutane Hydrate, as Determined by a Heat-Flow Calorimeter. *J Chem Thermodyn* **18** (10): 915–921. https://doi.org/10.1016/0021-9614(86)90149-7.

Hong, H. and Pooladi-Darvish, M. 2005. Numerical Study of Constant-Rate Gas Production from in Situ Gas Hydrate by Depressurization. In *Scientific Results from Malik 2002 Gas Hydrate Production Research Well Program, Mackenzie Delta, Northwest Territories, Canada*, eds. S. R. Dallimoreand T. S. Collett. Canada: Geological Survey of Canada.

Hoteit, H., Fahs, M., and Soltanian, MR. 2019. Assessment of CO_2 Injectivity During Sequestration in Depleted Gas Reservoirs. *Geosciences* **9** (5): 199. https://doi.org/10.3390/geosciences9050199.

Hussain, S. 2021. *Numerical Mechanistic Study of In-Situ CO_2 EOR - Kinetics and Recovery Performance Analysis*. Master thesis, University of Oklahoma, Norman, Oklahoma, USA.

Hussain, S., Ahmed, Z., Zakir, M. M. et al. 2023. Role of Temperature on the Performance of In-Situ CO_2 EOR. Paper presented at the SPE/PAPG Pakistan Section Annual Technical Symposium and Exhibition, Islamabad, Pakistan, 7−8 November. https://doi.org/10.2118/219495-MS.

Hussain, S., Wu, X., and Shiau, B. 2021. Numerical Mechanistic Study of In-Situ CO_2 EOR – Kinetics and Recovery Performance Analysis. Paper presented at the SPE Annual Technical Conference and Exhibition, Dubai, UAE, 21−23 September. https://doi.org/10.2118/206292-MS.

Janicki, G., Schlüter, S., Hennig, T. et al. 2011. Simulation of Methane Recovery from Gas Hydrates Combined with Storing Carbon Dioxide as Hydrates. *J Geol Res* **2011**: 1–15. https://doi.org/10.1155/2011/462156.

Kamath, V. A. 1984. *Study of Heat Transfer Characteristics During Dissociation of Gas Hydrates in Porous Media*. PhD Dissertation, Pittsburgh University, Pittsburgh, Pennsylvania, USA.

Kang, S.-P., Lee, H., and Ryu, B.-J. 2001. Enthalpies of Dissociation of Clathrate Hydrates of Carbon Dioxide, Nitrogen, (Carbon Dioxide+ Nitrogen), and (Carbon Dioxide + Nitrogen+ Tetrahydrofuran). *J Chem Thermodyn* **33** (5): 513–521. https://doi.org/10.1006/jcht.2000.0765.

Kim, H. C., Bishnoi, P. R., Heidemann, R. A. et al. 1987. Kinetics of Methane Hydrate Decomposition. *Chem Eng Sci* **42** (7): 1645–1653. https://doi.org/10.1016/0009-2509(87)80169-0.

Kumari, A., Madhaw, M., and Pendyala, VS. 2022. Prediction of Formation Conditions of Gas Hydrates Using Machine Learning and Genetic Programming. In *Advances in Human and Social Aspects of Technology. IGI Global*, ed. V. S. Pendyala, 200–224. Hershey: IGI Global. https://doi.org/10.4018/978-1-6684-4045-2.ch010.

Larson, SD. 1955. *Phase Studies of the Two-Component Carbon Dioxide-Water System Involving the Carbon Dioxide Hydrate*. PhD dissertation, University of Illinois, Urbana, Illinois, USA.

Lee, B. I. and Kesler, M. G. 1975. A Generalized Thermodynamic Correlation Based on Three-parameter Corresponding States. *AIChE J* **21** (3): 510–527. https://doi.org/10.1002/aic.690210313.

Lewis, J. 2022. *Chevron's Flagship Gorgon CCS Project Still Failing to Live up to Expectations*. upstreamonline.com. URL: https://www.upstreamonline.com/energy-transition/chevrons-flagship-gorgon-ccs-project-still-failing-to-live-up-to-expectations/2-1-1166185 (accessed 7 July 2024).

Lin, T.-K., Dahyar, M., Lee, M.-J. et al. 2020. Study of the Formation Mechanisms of CO_2 Hydrates from Matching the Experimental Data with a Porous Media Setting by Multiphase Flow-Geochemical-Thermal Reservoir Simulator. *J Taiwan Inst Chem Eng* **114**: 115–124. https://doi.org/10.1016/j.jtice.2020.09.015.

Long, J. P. 1994. *Gas Hydrate Formation Mechanism and Kinetic Inhibition*. PhD dissertation, Colorado School of Mines, Golden, Colorado, USA.

Machado, M. V. B., Delshad, M., and Sepehrnoori, K. 2023. Injectivity Assessment for CCS Field-Scale Projects with Considerations of Salt Deposition, Mineral Dissolution, Fines Migration, Hydrate Formation, and Non-Darcy Flow. *Fuel* **353**: 129148. https://doi.org/10.1016/j.fuel.2023.129148.

Marshall, D. R., Saito, S., and Kobayashi, R. 1964. Hydrates at High Pressures: Part I. Methane-Water, Argon-Water, and Nitrogen-Water Systems. *AIChE J* **10** (2): 202–205. https://doi.org/10.1002/aic.690100214.

Mathews, S. L., Servio, P. D., and Rey, A. D. 2020. Heat Capacity, Thermal Expansion Coefficient, and Grüneisen Parameter of CH_4, CO_2, and C_2H_6 Hydrates and Ice I_h via Density Functional Theory and Phonon Calculations. *Cryst Growth Des* **20** (9): 5947–5955.

Mathias, S. A., Gluyas, J. G., Oldenburg, C. M. et al. 2010. Analytical Solution for Joule–Thomson Cooling during CO_2 Geo-Sequestration in Depleted Oil and Gas Reservoirs. *Int J Greenh Gas Control* **4** (5): 806–810. https://doi.org/10.1016/j.ijggc.2010.05.008.

McLeod, H. O. and Campbell, J. M. 1961. Natural Gas Hydrates at Pressures to 10,000 Psia. *J Pet Technol* **13** (06): 590–594. https://doi.org/10.2118/1566-G-PA.

Moghanloo, R. G., Davudov, D., and Akita, E. 2018. Formation Damage by Organic Deposition. In *Formation Damage During Improved Oil Recovery*, eds. B. Yuan and D. A. Wood, Chap. 6, 243–273. New York: Elsevier. https://doi.org/10.1016/B978-0-12-813782-6.00006-3.

Moridis, G. J., Apps, J., Pruess, K. et al. 1998. EOSHYDR: A TOUGH2 Module for CH_4-Hydrate Release and Flow in the Subsurface. Report No.: LBNL-42386. Lawrence Berkeley National Laboratory, Berkeley, California, USA.

Moridis, G. J., Kowalsky, M. B., and Pruess, K. 2008. TOUGH+HYDRATE v1.0 User's Manual: A Code for the Simulation of System Behavior in HYDRATE Bearing Geologic Media. Lawrence Berkeley National Laboratory, Berkeley, California, USA.

Moridis, G. J., Queiruga, A. F., and Reagan, M. T. 2019. Simulation of Gas Production from Multilayered Hydrate-Bearing Media with Fully Coupled Flow, Thermal, Chemical and Geomechanical Processes Using TOUGH + Millstone. Part 1: Numerical Modeling of Hydrates. *Transp Porous Med* **128** (2): 405–430. https://doi.org/10.1007/s11242-019-01254-6.

Munck, J., Skjold-Jørgensen, S., and Rasmussen, P. 1988. Computations of the Formation of Gas Hydrates. *Chem Eng Sci* **43** (10): 2661–2672. https://doi.org/10.1016/0009-2509(88)80010-1.

Nakagawa, R., Hachikubo, A., and Shoji, H. 2008. Dissociation and Specific Heats of Gas Hydrates Under Submarine and Sublacustrine Environments. Paper presented at the International Conference on Gas Hydrates (ICGH), Vancouver, British Columbia, Canada, 6−10 July.

Nguyen, N. N., Galib, M., and Nguyen, A. V. 2020. Critical Review on Gas Hydrate Formation at Solid Surfaces and in Confined Spaces—Why and How Does Interfacial Regime Matter? *Eng Fuels* **34** (6): 6751–6760. https://doi.org/10.1021/acs.energyfuels.0c01291.

Ning, F. L., Glavatskiy, K., Ji, Z. et al. 2015. Compressibility, Thermal Expansion Coefficient and Heat Capacity of CH_4 and CO_2 Hydrate Mixtures Using Molecular Dynamics Simulations. *Phys Chem Chem Phys* **17** (4): 2869–2883. https://doi.org/10.1039/c4cp04212c.

NIST. n.d. NIST Chemistry WebBook. *Thermophysical Properties of Fluid Systems*. https://webbook.nist.gov/chemistry/fluid/.

Oldenburg, C. M. 2007. Joule-Thomson Cooling Due to CO_2 Injection into Natural Gas Reservoirs. *Energy Convers Manag* **48** (6): 1808–1815. https://doi.org/10.1016/j.enconman.2007.01.010.

Parrish, W. R. and Prausnitz, J. M. 1972. Dissociation Pressures of Gas Hydrates Formed by Gas Mixtures. *Ind Eng Chem Proc Des Dev* **11** (1): 26–35. https://doi.org/10.1021/i260041a006.

Redlich, O. and Kwong, J. N. S. 1949. On the Thermodynamics of Solutions; an Equation of State; Fugacities of Gaseous Solutions. *Chem Rev* **44** (1): 233–244. https://doi.org/10.1021/cr60137a013.

Roberts, O. L., Brownscombe, E. R., Howe, L. S. et al. 1941. Phase Diagrams of Methane and Ethane Hydrates. *Petr Eng* **12**.

Rose, S. K., Richels, R., Blanford, G. et al. 2017. The Paris Agreement and next Steps in Limiting Global Warming. *Climatic Change* **142** (1–2): 255–270. https://doi.org/10.1007/s10584-017-1935-y.

Ruppel, C. D. and Waite, W. F. 2020. Timescales and Processes of Methane Hydrate Formation and Breakdown, With Application to Geologic Systems. *JGR Solid Earth* **125** (8). https://doi.org/10.1029/2018JB016459.

Sartini, M. 2021. *High Pressure Vapor-Liquid Equilibrium Measurements of Methane and Water Mixtures Using Nuclear Magnetic Resonance Spectroscopy*. Master's thesis, Colorado State University, Fort Collins, Colorado, USA.

Shindo, Y., Lund, P. C., Fujioka, Y. et al. 1993a. Kinetics and Mechanism of the Formation of CO_2 Hydrate. *Int J Chem Kinet* **25** (9): 777–782. https://doi.org/10.1002/kin.550250908.

Shindo, Y., Lund, P. C., Fujioka, Y. et al. 1993b. Kinetics of Formation of CO_2 Hydrate. *Energy Convers Manag* **34** (9–11): 1073–1079. https://doi.org/10.1016/0196-8904(93)90055-F.

Sholihah, M. and Sean, W.-Y. 2021. Numerical Simulation on the Dissociation, Formation, and Recovery of Gas Hydrates on Microscale Approach. *Molecules* **26** (16): 5021. https://doi.org/10.3390/molecules26165021.

Shu, S.-S. and Lee, M.-J. 2016. Dynamic Behavior of Methane Hydrates Formation and Decomposition with a Visual High-Pressure Apparatus. *J Taiwan Inst Chem Eng* **62**: 1–9. https://doi.org/10.1016/j.jtice.2016.01.015.

Singh, R. P., Shekhawat, K. S., Das, M. K. et al. 2020. Geological Sequestration of CO_2 in a Water-Bearing Reservoir in Hydrate-Forming Conditions. *Oil Gas Sci Technol - Rev IFP Energies Nouvelles* **75**: 51. https://doi.org/10.2516/ogst/2020038.

Sloan Jr, E. D. and Koh, C. A. 2007. *Clathrate Hydrates of Natural Gases*, Third Edition. Boca Raton, Florida, USA: CRC Press.

Spycher, N., Pruess, K., and Ennis-King, J. 2003. CO_2-H_2O Mixtures in the Geological Sequestration of CO_2. I. Assessment and Calculation of Mutual Solubilities from 12 to 100°C and up to 600 Bar. *Geochim Cosmochim Acta* **67** (16): 3015–3031. https://doi.org/10.1016/S0016-7037(03)00273-4.

Stantec Consulting. 2010. *Quest Carbon Capture and Storage Project*, Vol. Volume 1: Project Description. Calgary, Alberta, Canada: Shell Canada Limited.

Sun, D., Ripmeester, J., and Englezos, P. 2016. Phase Equilibria for the $CO_2/CH_4/N_2/H_2O$ System in the Hydrate Region under Conditions Relevant to Storage of CO_2 in Depleted Natural Gas Reservoirs. *J Chem Eng Data* **61** (12): 4061–4067.

Takeya, S., Muromachi, S., Yamamoto, Y. et al. 2016. Preservation of CO_2 Hydrate under Different Atmospheric Conditions. *Fluid Phase Equilibria* **413**: 137–141. https://doi.org/10.1016/j.fluid.2015.10.036.

Uddin, M., Coombe, D., Law, D. et al. 2008a. Numerical Studies of Gas Hydrate Formation and Decomposition in a Geological Reservoir. *J Energy Resour Technol* **130** (3): 032501. https://doi.org/10.1115/1.2956978.

Uddin, M., Coombe, D., and Wright, F. 2008b. Modeling of CO_2-Hydrate Formation in Geological Reservoirs by Injection of CO_2 Gas. *J Energy Resour Technol* **130** (3): 032502. https://doi.org/10.1115/1.2956979.

van der Waals, J. H. and Platteeuw, J. C. 1958. Clathrate Solutions. In *Advances in Chemical Physics*, ed. I. Prigogine, 1–57. Hoboken, New Jersey, USA: John Wiley & Sons, Inc. https://doi.org/10.1002/9780470143483.

Verheggen, B., Strengers, B., Cook, J. et al. 2014. Scientists' Views about Attribution of Global Warming. *Environ Sci Technol* **48** (16): 8963–8971. https://doi.org/10.1021/es501998e.

Vinsome, P. K. W. and Westerveld, J. 1980. A Simple Method For Predicting Cap And Base Rock Heat Losses In' Thermal Reservoir Simulators. *J Can Pet Technol* **19** (03): 3. https://doi.org/10.2118/80-03-04.

Vlahakis, J. G., Chen, H.-S., Suwandi, M. S. et al. 1972. The Growth Rate of Ice Crystals: The Properties of Carbon Dioxide Hydrate, a Review of Properties of 51 Gas Hydrates. Report No.: 986391. Sycaruse University Department of Chemical Engineering and Materials Science.

Wapperom, M., Lyu, X., and Voskov, D. 2022. Accurate Modeling of Near-Wellbore Effects Induced by Supercritical CO_2 Injection. Paper presented at the ECMOR 2022, The Hague, Netherlands. https://doi.org/10.3997/2214-4609.202244092.

Wu, X., Dai, L., Chang, Q. et al. 2023. Study of Controlling Parameters of In-Situ CO_2 EOR Using Numerical Simulations. Paper presented at the SPE Western Regional Meeting, Anchorage, Alaska, USA, 22−25 May. https://doi.org/10.2118/213010-MS.

Xu, J., Chen, Z., and Li, R. 2020. Impacts of Pore Size Distribution on Gas Injection in Intraformational Water Zones in Oil Sands Reservoirs. *Oil Gas Sci Technol - Rev IFP Energies Nouvelles* **75**: 75. https://doi.org/10.2516/ogst/2020047.

Yamada, K., Fernandes, B. R. B., Kalamkar, A. et al. 2024. Development of a Hydrate Risk Assessment Tool Based on Machine Learning for CO_2 Storage in Depleted Gas Reservoirs. *Fuel* **357**: 129670. https://doi.org/10.1016/j.fuel.2023.129670.

Yoon, J.-H., Yamamoto, Y., Komai, T. et al. 2003. Rigorous Approach to the Prediction of the Heat of Dissociation of Gas Hydrates. *Ind Eng Chem Res* **42** (5): 1111–1114. https://doi.org/10.1021/ie020598e.

You, K., Flemings, P. B., Malinverno, A. et al. 2019. Mechanisms of Methane Hydrate Formation in Geological Systems. *Rev Geophys* **57** (4): 1146–1196. https://doi.org/10.1029/2018RG000638.

Zatsepina, O. Y. and Pooladi-Darvish, M. 2011. CO_2 -Hydrate Formation in Depleted Gas Reservoirs–A Methodology for CO_2 Storage. *Energy Procedia* **4**: 3949–3956. https://doi.org/10.1016/j.egypro.2011.02.334.

Zatsepina, O. Y. and Pooladi-Darvish, M. 2012. Storage of CO_2 as Hydrate in Depleted Gas Reservoirs. *SPE Res Eval & Eng* **15** (1): 98–108. https://doi.org/10.2118/137313-PA.